NACA

RESEARCH MEMORANDUM

for the

Bureau of Aeronautics, Navy Department

AERODYNAMIC CHARACTERISTICS OF A 0.5-SCALE MODEL OF THE FAIRCHILD XSAM-N-2 LARK MISSILE AT HIGH SUBSONIC SPEEDS

(TED No. NACA DE322)

By Andrew Martin and Harlo A. Hunter

Ames Aeronautical Laboratory
Moffett Field, Calif.

NATIONAL ADVISORY COMMITTEE
FOR AERONAUTICS

WASHINGTON

September 28, 1949

NATIONAL ADVISORY COMMITTEE FOR AERONAUTICS

RESEARCH MEMORANDUM

for the

Bureau of Aeronautics, Navy Department

AERODYNAMIC CHARACTERISTICS OF A 0.5-SCALE MODEL OF THE FAIRCHILD XSAM-N-2 LARK MISSILE AT HIGH SUBSONIC SPEEDS

(TED No. NACA DE322)

By Andrew Martin and Harlo A. Hunter

SUMMARY

An investigation was conducted to determine the longitudinal- and lateral-stability characteristics of a 0.5-scale model of the Fairchild Lark missile. The model was tested with 0° and with 22.5° of roll. Three horizontal wings having NACA 16-009, 16-209, and 64A-209 sections were tested. Pressures were measured on both pointed and blunt noses.

The wind-tunnel-test data indicate that rolling the missile 22.5° had no serious effect on the static longitudinal stability. The desired maneuvering acceleration could not be attained with any of the horizontal wings tested, even with the horizontal wing flaps deflected 50°. The flaps on the 64A-209 wing (with small trailing-edge angles and flat sides) were effective at all flap deflections, while the flaps on the 16-series wings (with large trailing-edge angles) lost effectiveness at small flap deflections. The data showed that rolling moment existed when the vertical wing flaps were deflected with the model at other than zero angle of attack. A similar rolling moment probably would be found with the horizontal wing flaps deflected and the model yawed.

INTRODUCTION

Tests were conducted in the Ames 16-foot high-speed wind tunnel of a 0.5-scale model of the Fairchild Lark (XSAM-N-2) pilotless aircraft in order to evaluate the longitudinal- and lateral-stability characteristics and to measure the nose pressures at high subsonic speeds. A wing with the NACA 64A-209 section was included in these tests as an alternate horizontal wing because previous tests had indicated a marked improvement in the high-speed aerodynamic characteristics of controls when the trailing-edge angle was reduced and the sides flattened near the trailing edge. (See reference 1.) This investigation was made at the request of the Bureau of Aeronautics, Navy Department.

The Lark missile is a ship-to-air type and is designed to be flown at zero angle of attack, at zero yaw, and at zero roll. Departures from these zero angles are indicated by pressure differentials set up at the orifices on the nose. The cruciform-tail control surfaces function as both rudders and elevators. The stabilizers have a fixed angle of incidence while the ruddervators are movable. The horizontal wing flaps are used to provide lift control; whereas the vertical wing flaps are utilized for turns. Zero roll is maintained by means of ailerons which intermittently project from the wing tips. One pair of ailerons is set to produce a clockwise rolling moment while the other pair produces a counterclockwise moment. However, aileron tests were not included in this investigation.

It is desired that the missile be capable of performing 4 g turns at 0° angle of attack and of attaining a maximum speed of 590 miles per hour (0.85 Mach number) at an altitude of 25,000 feet, with a powered-flight endurance of approximately 4 minutes and a range of approximately 40 statute miles in order to permit the interception of enemy bombers approaching at 25,000 feet and 300 miles per hour. (See reference 2.)

SYMBOLS

C_L lift coefficient $\left(\frac{\text{lift}}{qS}\right)$

C_D drag coefficient $\left(\frac{\text{drag}}{qS}\right)$

C_m pitching-moment coefficient about the 20-percent-chord line of the wing $\left(\frac{\text{pitching moment}}{qSc}\right)$

C_l rolling-moment coefficient $\left(\frac{\text{rolling moment}}{qSb}\right)$

S wing area, square feet

W_h horizontal wing

W_v vertical wing

c wing chord, feet

c_t tail chord, feet

q	dynamic pressure $\left(\frac{1}{2}\rho V^2\right)$, pounds per square foot
b	wing span, feet
α	angle of attack of fuselage center line, degrees
δ_{f_h}	deflection of horizontal wing flaps relative to the horizontal wing, degrees
δ_{f_v}	deflection of vertical wing flaps relative to the vertical wing, degrees
δ_{f_t}	deflection of the ruddervators relative to the fixed portions of the tail surfaces, degrees
i_t	incidence of tail surfaces relative to fuselage, degrees
M	Mach number, ratio of the free-stream velocity to the velocity of sound
P	pressure coefficient $\left(\frac{p-p_o}{q}\right)$
p	local static pressure, pounds per square foot
p_o	free-stream static pressure, pounds per square foot

MODEL AND APPARATUS

The 0.5-scale model used for this investigation was geometrically similar to the full-scale Lark pilotless aircraft. The model in its complete configuration included horizontal and vertical wings, fuselage, and tail assembly as shown in figure 1. The vertical and horizontal wings normally had NACA 16-009 and NACA 16-209 sections, respectively, with 20-percent-chord plain flaps. The tail was of cruciform arrangement with NACA 16-008 sections; each tail surface had a stabilizer and a 20-percent-chord ruddervator. Table I lists the pertinent dimensions of the model. The fuselage was circular in cross section. The normal fuselage nose was pointed and the alternate nose was blunt. (See fig. 2.)

Two alternate horizontal wings with NACA 16-009 and NACA 64A-209 sections were also tested. The trailing-edge angles for all three horizontal wings and also for the tail surfaces (16-008 section) are listed in table I. The wing flaps and ruddervators were set manually during tunnel shutdowns.

Figure 3 shows the Lark model mounted in the Ames 16-foot high-speed wind tunnel on the sting-support system. Aerodynamic forces and

moments on the model were measured by means of an electrical strain-gage balance mounted on the upstream end of the sting and housed within the model fuselage. The support system was arranged so that the moment center of the model remained on the horizontal center line of the wind tunnel. The angle of attack was measured by means of a pendulum-type angle-of-attack indicator mounted within the fuselage.

TESTS

Tests were conducted through a Mach number range from 0.40 to 0.91. The corresponding Reynolds number range under the test conditions was 2.2 to 3.6 million based on the wing chord. Lift, drag, pitching moment, and rolling moment were measured for angles of attack from -6° to 16°. The model configurations tested are presented in table II. The horizontal and vertical wing flaps, the ruddervators, and the stabilizers were deflected as follows:

Control Surfaces	Deflection
Horizontal flaps	-50° to $+50^\circ$ (positive down)
Vertical flaps	0°, $+10^\circ$, $+20^\circ$ (positive left)
Ruddervators	0°, -5°, -10°, -15° (positive down)
Stabilizers	0°, -3°, $+3^\circ$ (positive down)

CORRECTIONS

Tunnel-wall and constriction corrections were applied to the results in this report. The tunnel-wall corrections were calculated by the method of reference 3 and the constriction corrections were evaluated using the method developed in reference 4. The tunnel-wall corrections, based on the area of the horizontal wing, are as follows:

$$\alpha = \alpha_u + 0.142\, C_L$$

$$C_D = C_{D_u} + 0.00248\, C_L^2$$

$$C_m = C_{m_u} + 0.00557\, C_L \text{ (for tail on)}$$

where subscript u denotes uncorrected value.

Fuselage base pressures were measured, but due to their erratic variation with both Mach number and angle of attack no corrections were applied to the drag data. The measured base pressures always exceeded free-stream static pressure.

RESULTS AND DISCUSSION

An index showing the model configurations, the control settings, and the plotted coefficients for all the figures which present test data is shown in table II.

Lift Characteristics

Figure 4(a) is a plot in carpet form showing the variation of lift coefficient with angle of attack, for various Mach numbers, of the complete model in the unrolled attitude. Between 0° and -2° angle of attack a definite break or change of slope may be seen in most of the lift curves. This reduction in slope is attributed to either a sudden shift in transition (references 5 and 6) or to inaccuracies in measuring small lift forces with the 4000-pound-capacity strain-gage. Above 0.80 Mach number the slopes of the lift curves are greater in the negative angle-of-attack range below the break than at the positive angles of attack.

The breaks in the lift curves at approximately 8° angle of attack can be explained with the aid of visual tuft data which show that separation occurred over the inboard portion of the wing on the upper surface when the model reached this angle of attack. As the flow over the wing tips and over the fuselage remained smooth at the higher angles of attack, the lift coefficient continued to increase, but at a reduced rate.

Comparison of the lift curves for the model in the unrolled attitude (fig. 4(a)) with the lift curves for the model rolled 22.5° (fig. 4(b)) reveals that the lift-curve slopes are approximately the same for positive angles of attack up to 8°; however, with the model rolled 22.5° the magnitude of the lift coefficient was generally less, below 8° angle of attack, at the higher test Mach numbers.

The lift curves for the model with the tail off and with the three different horizontal wings are shown in figures 5(a) and 5(b). The slopes of the lift curves and the angles of attack at the stall were generally about the same for all three wings. The tufts again showed that the wing tips and the fuselage were not stalled even at the highest test angle of attack. Definite irregularities in the lift curves for each wing tested are apparent at small angles of attack. The 64A-209 wing developed greater lift than the other wings at all test Mach numbers and all angles of attack. Lift curves for the 16-009 wing do not pass through zero lift coefficient at zero angle of attack as would be expected with the symmetrical sections. This discrepancy may have been caused by malfunctioning of the angle-of-attack indicator.

Drag Characteristics

Figures 6(a) and 6(b) are plots in carpet form of lift coefficient versus drag coefficient at constant Mach numbers for the model (W_h, 16-209; W_v, 16-009) both unrolled and rolled 22.5°. Figures 7(a) and 7(b) show the variations of lift coefficient with drag coefficient at various Mach numbers for the three horizontal wings tested.

The variations of drag coefficient with Mach number at constant angles of attack, for the model both unrolled and rolled 22.5°, are shown in figures 8(a) and 8(b), respectively. These curves indicate that a minimum drag coefficient of about 0.024 was measured at a Mach number of approximately 0.80 for the model in both the normal and the rolled flight attitudes.

The drag characteristics of the model with the tail removed and with three different horizontal wings are shown in figure 9. The Mach number for drag divergence, defined as the Mach number at which $\frac{\partial C_D}{\partial M}$ is 0.10, was slightly less for the 64A-209 wing than for the 16-series wings. However, at positive lift coefficients, the drag coefficient for the 64A-209 wing was less than for either the 16-009 or 16-209 wing over a major portion of the test Mach number range.

Pitching-Moment Characteristics

Figure 10(a) shows, in carpet form, the variation of pitching-moment coefficient with lift coefficient for the Mach number range of the tests. These curves show irregularities corresponding to the irregularities of the lift curves (fig. 4(a)) at the same angle of attack. Figures 10(a) and 10(b) show that rolling the model 22.5° had no serious effect on the static longitudinal stability.

Pitching-moment-coefficient curves for the model with the tail surfaces removed and with each of the three horizontal wings are presented in figure 11. With any of the three wings the model tended to become less unstable with increase in Mach number. At any one Mach number the slopes of the curves for the three wings are about the same. At all Mach numbers and lift coefficients, the 64A-209 wing gave the largest negative pitching-moment coefficient of the three wings tested.

Flap Characteristics

Horizontal flaps.- The increments of lift and pitching-moment coefficients due to the deflected wing flaps at various Mach numbers are shown in figures 12 and 13, respectively. These figures illustrate

that the wing flap effectiveness in producing lift and pitching moment was good for the 64A-209 wing at all flap deflections and Mach numbers. The flaps on the 16-209 wing lost their effectiveness at small flap deflections at all Mach numbers but regained their effectiveness with further increase of flap deflection. The more limited data indicate similar tendencies for small flap deflections on the 16-009 wing. The improved effectiveness of the flaps on the 64A-209 wing can be attributed to the smaller trailing-edge angle. (See reference 1.)

Figure 14 shows the variation of drag-coefficient increments with Mach number at constant flap deflections for the three wings tested. The increment of drag coefficient for a given flap deflection was less for the 16-009 wing than for either of the other wings.

Horizontal and vertical flaps.- Presented in figure 15 is the variation of drag coefficient with Mach number for various combinations of horizontal and vertical flap deflections. The curves of rolling-moment-coefficient variation with Mach number, figure 16, show changes in rolling moment with angle of attack when the vertical wing flaps were deflected. These changes were probably due to differences in effectiveness between the upper and lower wing flaps when one vertical wing was in the wake of the forward part of the fuselage.

Tail Characteristics

The curves of pitching-moment-coefficient increment due to the deflection of the ruddervators (fig. 17) indicate a large decrease in pitching moment as the Mach number increased from 0.80 to 0.825. This loss in ruddervator effectiveness is similar to the loss in wing flap effectiveness at small flap deflections for the 16-209 wing. (See fig. 12.)

The pitching-moment-coefficient increments due to various stabilizer incidences at constant Mach numbers are shown in figure 18. The curves in figure 19 show the effects of Mach number, of horizontal wings, and of horizontal wing flaps on the stabilizer-effectiveness parameter $\left(\frac{\partial C_m}{\partial i_t}\right)_{\alpha = 0^\circ}$. These curves were obtained from plots similar to figure 18 but for other flap deflections.

The figures showing the variation of lift coefficient with pitching-moment coefficient due to horizontal flap deflection for various ruddervator deflections (fig. 20) and stabilizer settings (fig. 21) are included for use in determining the stabilizer setting and ruddervator deflection necessary to trim the missile at the design Mach number of 0.85.

Performance Objective

One performance objective of the Lark missile is that it be capable of attaining a 4 g maneuvering acceleration while flying with the body at 0° angle of attack at a Mach number of 0.85 at 25,000 feet altitude with one-quarter fuel load. The weight of the missile with this fuel load is 910 pounds and the center of gravity is at 20 percent of the wing chord. (See reference 2.) Flight accelerations were calculated using test data for the model trimmed at zero angle of attack with the horizontal wing flaps deflected 50° (fig. 20). The data indicate that the missile with the 16-209 wing could attain a maneuvering acceleration of 2.7 g, and that with the 64A-209 wing it could attain an acceleration of 3.0 g under these conditions.

Nose Pressures

The pressures over the nose of the model (figs. 22, 23, and 24) were recorded primarily for use in the development of the angle-of-attack stabilization system of the missile.

CONCLUSIONS

The high-speed wind-tunnel tests of the 0.5-scale model of the Fairchild Lark indicated the following:

1. Rolling this missile 22.5° has no serious effect on the static longitudinal stability.

2. The missile with the test model configuration will not attain the desired maneuvering accelerations even with the horizontal wing flaps deflected 50°.

3. The wake due to the forward portion of the fuselage causes a rolling moment when the vertical wing flaps are deflected with the missile at angles of attack other than 0°. A similar rolling moment probably exists with the horizontal wing flaps deflected when the missile is sideslipping or yawed.

4. The flaps on the NACA 16-series wings were ineffective at small deflections, particularly at the higher Mach numbers. Substitution of the NACA 64A-209 sections alleviated this condition because of the smaller trailing-edge angle.

Ames Aeronautical Laboratory,
National Advisory Committee for Aeronautics,
Moffett Field, Calif.

REFERENCES

1. Axelson, John A.: A Summary and Analysis of Wind-Tunnel Data on the Lift and Hinge-Moment Characteristics of Control Surfaces up to a Mach Number of 0.90. NACA RM A7L02, 1948.

2. Anon.: Survey of Project Activities during September and October, 1948. The Fairchild Lark Projects - Models XSAM-N-2 and XSAM-N-2a. Fairchild Report IL-523, Dec., 1948.

3. Silverstein, Abe, and White, James A.: Wind-Tunnel Interference with Particular Reference to Off-Center Positions of the Wing and to the Downwash at the Tail. NACA Rep. 547, 1935.

4. Herriot, John G.: Blockage Corrections for Three-Dimensional-Flow Closed-Throat Wind Tunnels, with Consideration of the Effect of Compressibility. NACA RM A7B28, 1947.

5. Holstein, H.: Maintaining the Laminar Conditions by Means of the Shape (Laminar Profile). AVA Monographs, ed. by A. Betz. B. Boundary layer, ed. by W. Tollmien, Sec. 4.1, pp. 1 - 17. Map Report and Translation 1005, Apr. 1, 1948.

6. Lindsey, W. F., Stevenson, D. B., and Daley, Bernard N.: Aerodynamic Characteristics of 24 NACA 16-Series Airfoils at Mach Numbers Between 0.3 and 0.8. NACA TN 1546, 1948.

TABLE I.- DIMENSIONS OF 0.5-SCALE MODEL OF THE XSAM-N-2 FAIRCHILD LARK

Fuselage	
Length, over-all, feet	7.344
Diameter, maximum, feet	0.708
Wings	
Span, feet	3.092
Chord, constant, feet	0.883
Mean aerodynamic chord, feet	0.883
Angle of incidence, degrees	0
Dihedral, degrees	0
Section, horizontal wing	NACA 16-209
Trailing-edge angle, degrees	22
Section, vertical wing and alternate horizontal wing	NACA 16-009
Trailing-edge angle, degrees	22
Section, second alternate horizontal wing	NACA 64A-209
Trailing-edge angle, degrees	10.7
Area, square feet	2.73
Aspect ratio	3.50
Sweep, degrees	0
Flap span (each), feet	1.143
Flap chord (20 percent c), feet	0.177
Tail Surfaces	
Span (in plane of surface), feet	2.021
Chord, constant, feet	0 642
Angle of incidence, degrees	0 (alternate ±3)
Dihedral, degrees	45
Section	NACA 16-008
Trailing-edge angle, degrees	19.6
Area (in plane of surface), square feet	1.30
Sweepback degrees	1.6
Ruddervator span (each), feet	0.571
Ruddervator chord (20 percent c_t), feet	0.128
Tail length, feet	3.05

TABLE II.- TEST-DATA FIGURE INDEX

Model Configuration								Figure number											
Horizontal wing	Vertical wing	Horizontal wing flaps (deg)	Vertical wing flaps (deg)	Stabilizers (deg)	Rudder-vators (deg)	Nose	Attitude	C_L vs α	C_l vs C_D	C_D vs M	C_L vs C_m	ΔC_L vs δ_{f_h}	ΔC_m vs δ_{f_h}	ΔC_D vs M	C_l vs M	ΔC_m vs δ_{f_t}	ΔC_m vs i_t	$\left(\frac{\delta C_m}{\delta i_t}\right)_{\alpha=0}$ vs M	P vs α
16-209	16-009	0	0	0	0	Normal	Unrolled	4(a)	6(a)	8(a)	10(a)								
16-209	16-009	0	0	0	0	Normal	Rolled 22.5°	4(b)	6(b)	8(b)	10(b)								
16-209	16-009	0	0	off	off	Normal	Unrolled	5(a) 5(b)	7(a) 7(b)	9	11								
64A-209	16-009	0	0	off	off	Normal	Unrolled	5(a) 5(b)	7(a) 7(b)	9	11								
16-009	64A-209	0	0	off	off	Normal	Unrolled	5(a) 5(b)	7(a) 7(b)	9	11								
16-209	16-009	-20 to +50	0	off	off	Normal	Unrolled					12(a)	13(a)	14(a)					
64A-209	16-009	-20 to +50	0	off	off	Normal	Unrolled					12(b)	13(b)	14(b)					
16-009	64A-209	0 to +50	0	off	off	Normal	Unrolled					12(c)	13(c)	14(c)					
16-209	16-009	-50 to +50	0 to 20	0	0	Normal	Unrolled			15					16				
16-209	16-009	0	0	0	0 to -15	Normal	Unrolled									17			
16-209	16-009	0	0	-3 to +3	0	Normal	Unrolled										18		
16-209 and off	16-009 and off	-50 to +50	0	-3 to +3	0	Normal	Unrolled											19	
16-209	16-009	-50 to +50	0	0	0 to -10	Normal	Unrolled				20								
16-209	16-009	-50 to +50	0	-3 to +3 and off	0 and off	Normal	Unrolled				21								
16-209	16-009	10 and 30	0	0	0	Normal	Unrolled												22 23
16-209	16-009	0	0	0	0	Alter-nate	Unrolled												24

FIGURE LEGENDS

Figure 1.– The 0.5–scale model of the XSAM–N–2 Fairchild Lark.

Figure 2.– Location of nose pressure orifices. (a) Normal and alternate noses with orifices 45° from the vertical plane. (b) Normal nose with orifices on horizontal and vertical planes.

Figure 3.– Photograph of the 0.5–scale model XSAM–N–2 Lark in the Ames 16–foot high–speed wind tunnel. (a) Front view. (b) Rear view.

Figure 4.– Variation of lift coefficient with angle of attack. δ_{f_h}, δ_{f_v}, δ_{f_t}, $i_t = 0°$; W_h, 16–209, W_v, 16–009. (a) Unrolled.

Figure 4.– Concluded. (b) Rolled 22.5°.

Figure 5.– Variation of lift coefficient with angle of attack for the model with three different horizontal wings, less tail. δ_{f_h}, $\delta_{f_v} = 0°$. (a) M, 0.40, 0.65, 0.75, 0.80.

Figure 5.– Concluded. (b) M, 0.825, 0.85, 0.875, 0.90, 0.91.

Figure 6.– Variation of lift coefficient with drag coefficient at various Mach numbers. δ_{f_h}, δ_{f_v}, δ_{f_t}, $i_t = 0°$; W_h, 16–209; W_v, 16–009. (a) Unrolled.

Figure 6.– Concluded. (b) Rolled 22.5°.

Figure 7.– Variation of lift coefficient with drag coefficient for the model with three different horizontal wings, less tail. δ_{f_h}, $\delta_{f_v} = 0°$. (a) M, 0.40, 0.65, 0.75, 0.80.

Figure 7.– Concluded. (b) M, 0.825, 0.85, 0.875, 0.90, 0.91.

Figure 8.– Variation of drag coefficient with Mach number at various angles of attack. δ_{f_h}, δ_{f_v}, δ_{f_t}, $i_t = 0°$; W_h, 16–209, W_v, 16–009. (a) Unrolled.

Figure 8.– Concluded. (b) Rolled 22.5°.

Figure 9.– Variation of drag coefficient with Mach number for the model with three different horizontal wings, less tail. δ_{f_h}, $\delta_{f_v} = 0°$.

Figure 10.– Variation of lift coefficient with pitching–moment coefficient. δ_{f_h}, δ_{f_v}, δ_{f_t}, $i_t = 0°$; W_h, 16–209, W_v, 16–009. (a) Unrolled.

Figure 10.– Concluded. (b) Rolled 22.5°.

Figure 11.– Variation of lift coefficient with pitching-moment coefficient for the model with three different horizontal wings, less tail. δ_{f_h}, $\delta_{f_v} = 0^\circ$.

Figure 12.– Variation of lift-coefficient increment with horizontal flap deflection for three different horizontal wings, model less tail. α, $\delta_{f_v} = 0^\circ$. (a) Horizontal wing 16-009. (b) Horizontal wing 16-209. (c) Horizontal wing 64A-209.

Figure 13.– Variation of pitching-moment-coefficient increment with horizontal wing-flap deflection for three different horizontal wings, model less tail α, $\delta_{f_v} = 0^\circ$. (a) Horizontal wing 16-009. (b) Horizontal wing 16-209. (c) Horizontal wing 64A-209.

Figure 14.– Variation of drag-coefficient increment with Mach number due to horizontal flap deflections for three different horizontal wings, model less tail α, $\delta_{f_v} = 0^\circ$. (a) Horizontal wing 16-009. (b) Horizontal wing 16-209. (c) Horizontal wing 64A-209.

Figure 15.– Variation with Mach number of drag coefficient for various combinations of horizontal- and vertical-flap deflections. α, δ_{f_t}, $i_t = 0^\circ$; W_h, 16-209, W_v, 16-009.

Figure 16.– Variation of rolling-moment coefficient with Mach number for various angles of attack with various combinations of horizontal- and vertical-flap deflections. δ_{f_t}, $i_t = 0^\circ$; W_h, 16-209, W_v, 16-009. (a) δ_{f_v}, 10°; δ_{f_h}, -30°. (b) δ_{f_v}, 10°; δ_{f_h}, 30°. (c) δ_{f_v}, 10°; δ_{f_h}, 20°. (d) δ_{f_v}, 20°; δ_{f_h}, 30°. (e) δ_{f_v}, 20°; δ_{f_h}, 20°.

Figure 17.– Pitching-moment-coefficient increments due to rudder-vator deflections at various Mach numbers. α, δ_{f_h}, δ_{f_v}, $i_t = 0^\circ$; W_h, 16-209, W_v, 16-009.

Figure 18.– Pitching-moment-coefficient increments due to tail incidence variation at various Mach numbers. α, δ_{f_h}, δ_{f_v}, $\delta_{f_t} = 0^\circ$; W_h, 16-209, W_v, 16-009.

Figure 19.– Variation of stabilizer effectiveness with Mach number for several wing flap deflections and with the wings off. α, δ_{f_t}, $\delta_{f_v} = 0^\circ$; W_h, 16-209, W_v, 16-009.

Figure 20.– Variation of pitching-moment coefficient with lift coefficient for various deflections of horizontal wing flaps and rudder-vators at a Mach number of 0.85. α, δ_{f_v}, $i_t = 0^\circ$; W_h, 16-209, W_v, 16-009.

Figure 21.- Variation of pitching-moment coefficient with lift coefficient for various tail incidences and horizontal wing-flap deflections at a Mach number of 0.85, with and without tail. α, δ_{f_v}, $\delta_{f_t} = 0°$; W_h, 16-209, W_v, 16-009.

Figure 22.- Variation of pressure coefficient with angle of attack at various nose orifices of the normal nose. Orifices 45° to vertical plane as shown in figure 2(a). (a) Orifice A. (b) Orifice B. (c) Orifice C.

Figure 22.- Concluded. (d) Orifice D. (e) Orifice E.

Figure 23.- Variation of pressure coefficient with angle of attack at various nose orifices of the normal nose. Orifices in horizontal and vertical planes as shown in figure 2(b). (a) Orifice A'. (b) Orifice B'. (c) Orifice D'.

Figure 23.- Concluded. (d) Orifice C'. (e) Orifice E'.

Figure 24.- Variation of pressure coefficient with angle of attack at various nose orifices of the alternate nose. Orifices 45° to vertical plane as shown in figure 2(a). (a) Orifice A. (b) Orifice B. (c) Orifice C.

Figure 24.- Concluded. (d) Orifice D. (e) Orifice E.

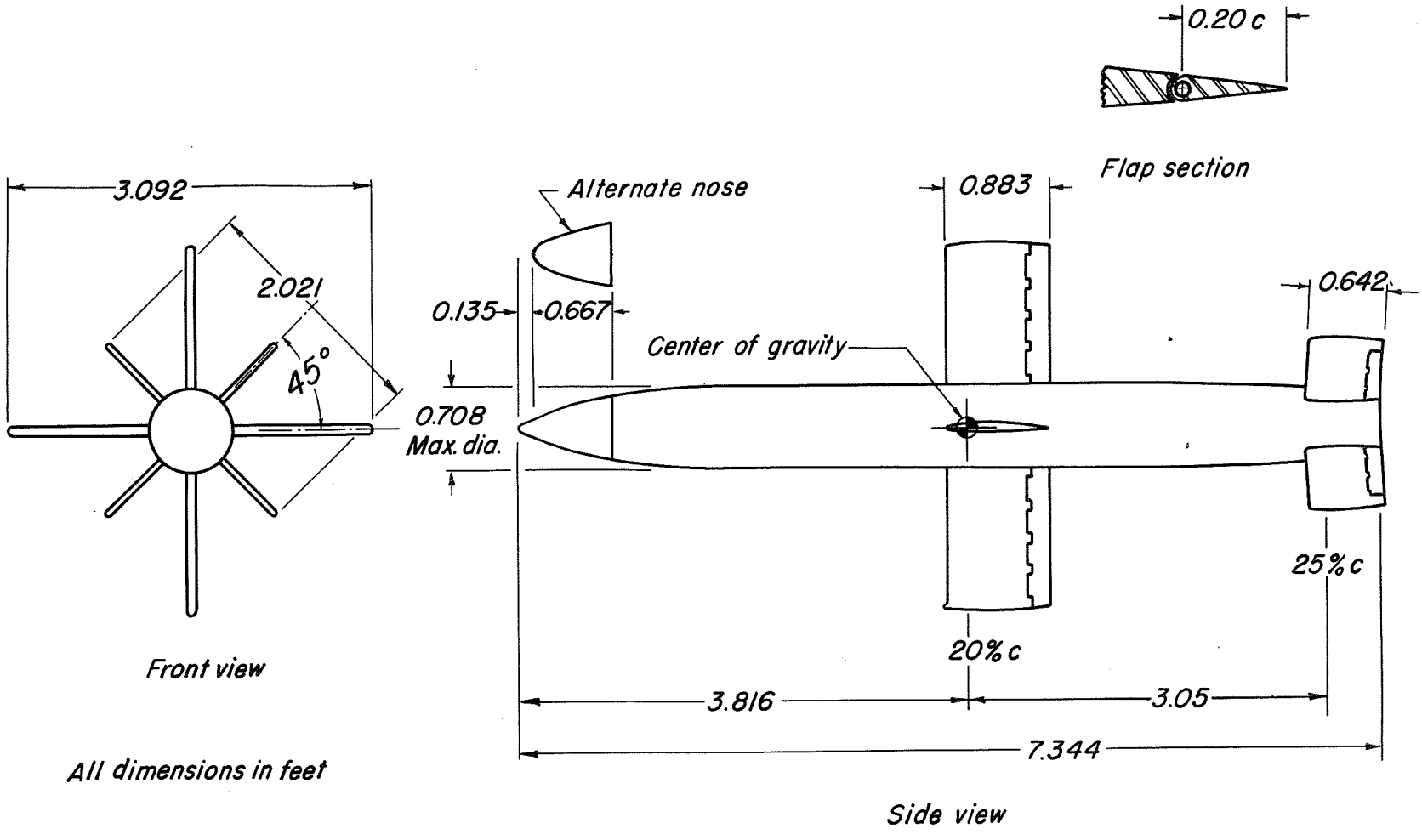

Figure I. - The 0.5-scale model of the XSAM-N-2 Fairchild Lark.

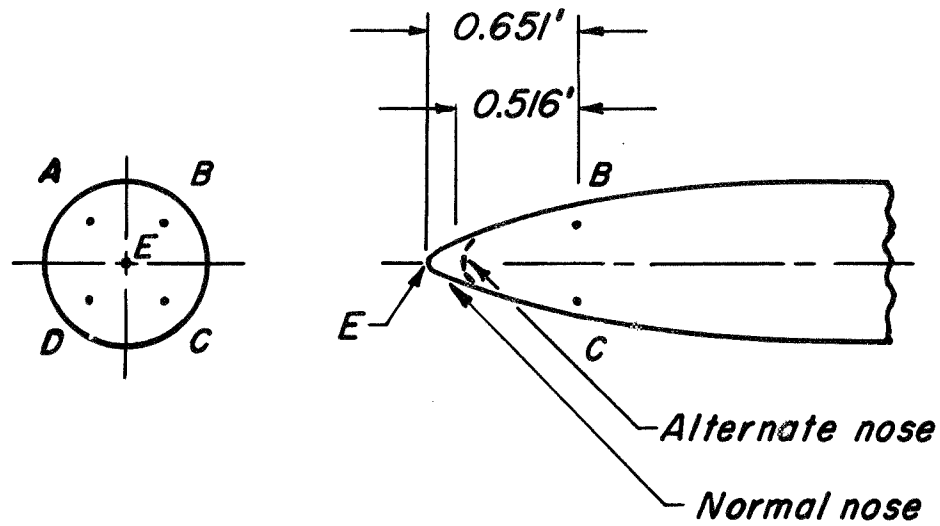

Front view Side view

(a) Normal and alternate noses with orifices 45° from the vertical plane.

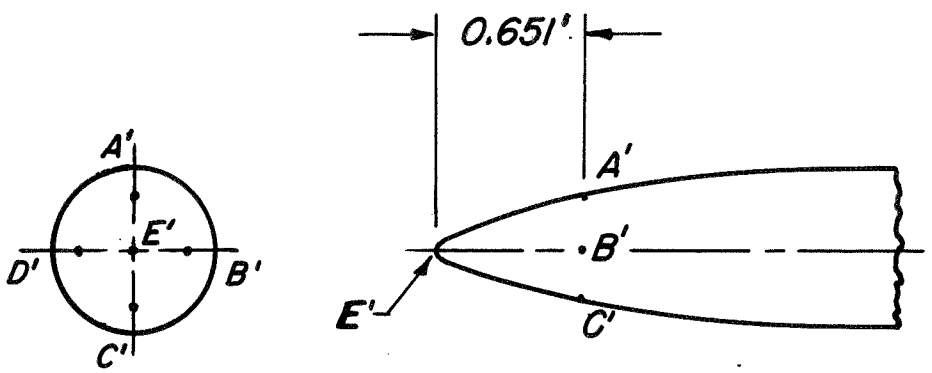

Front view Side view

(b) Normal nose with orifices on horizontal and vertical planes.

Figure 2.- Location of nose pressure orifices.

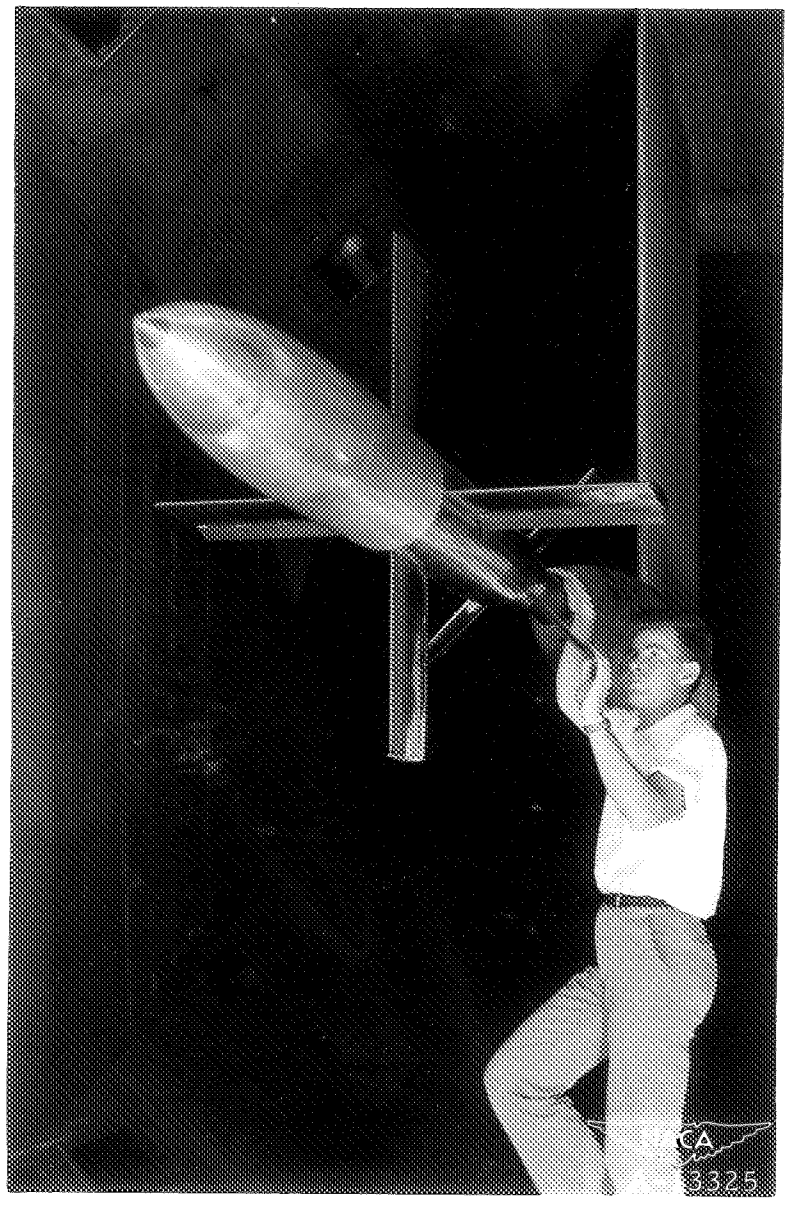

(a) Front view.

(b) Rear view.

Figure 3.- Photograph of the 0.5-scale model XSAM-N-2 Lark in the Ames 16-foot high-speed wind tunnel.

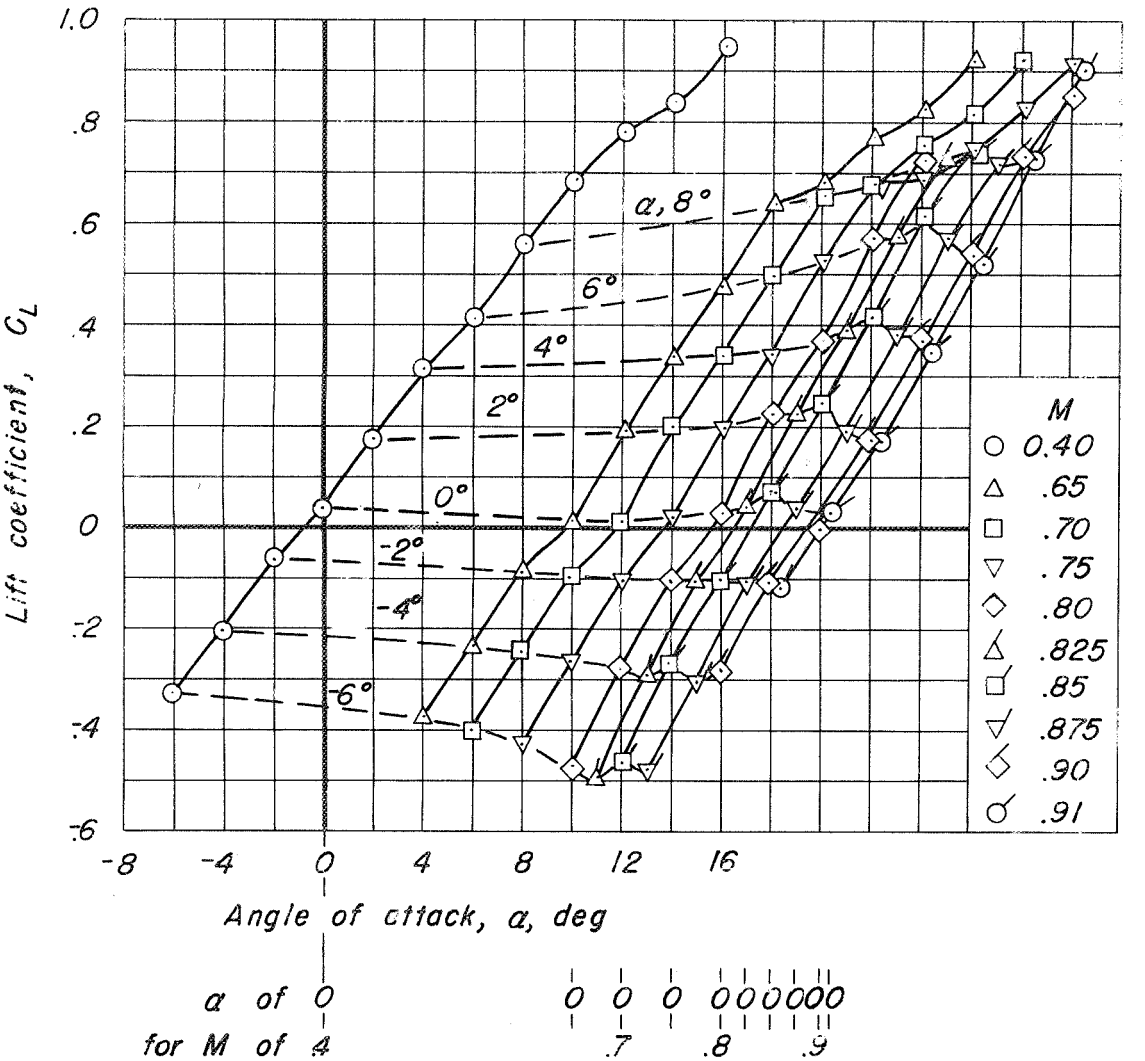

(a) Unrolled.

Figure 4.- Variation of lift coefficient with angle of attack. δ_{f_h}, δ_{f_v}, δ_{f_t}, $i_t = 0°$; W_h, 16-209, W_v, 16-009.

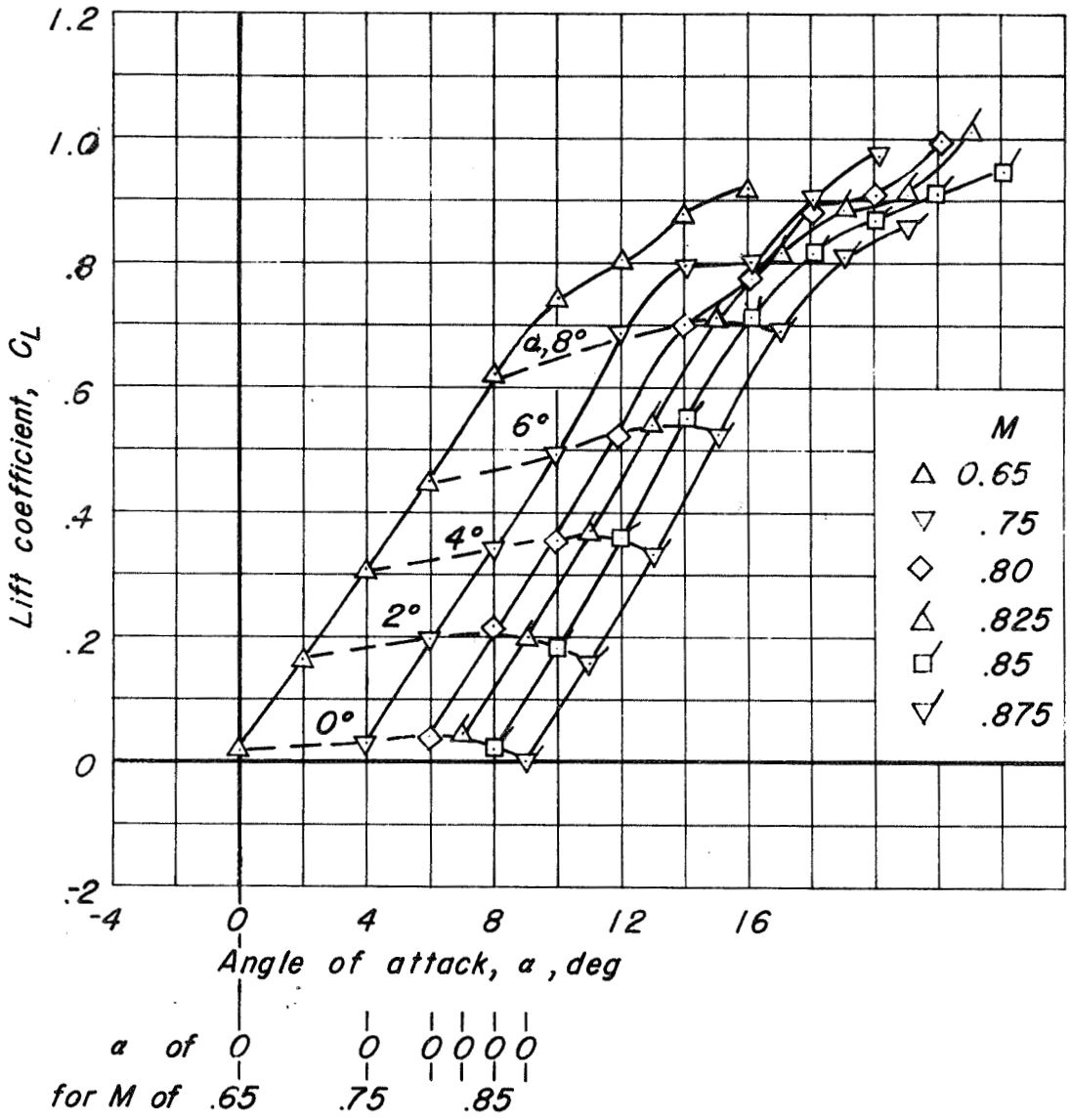

(b) Rolled 22.5°.

Figure 4.- Concluded.

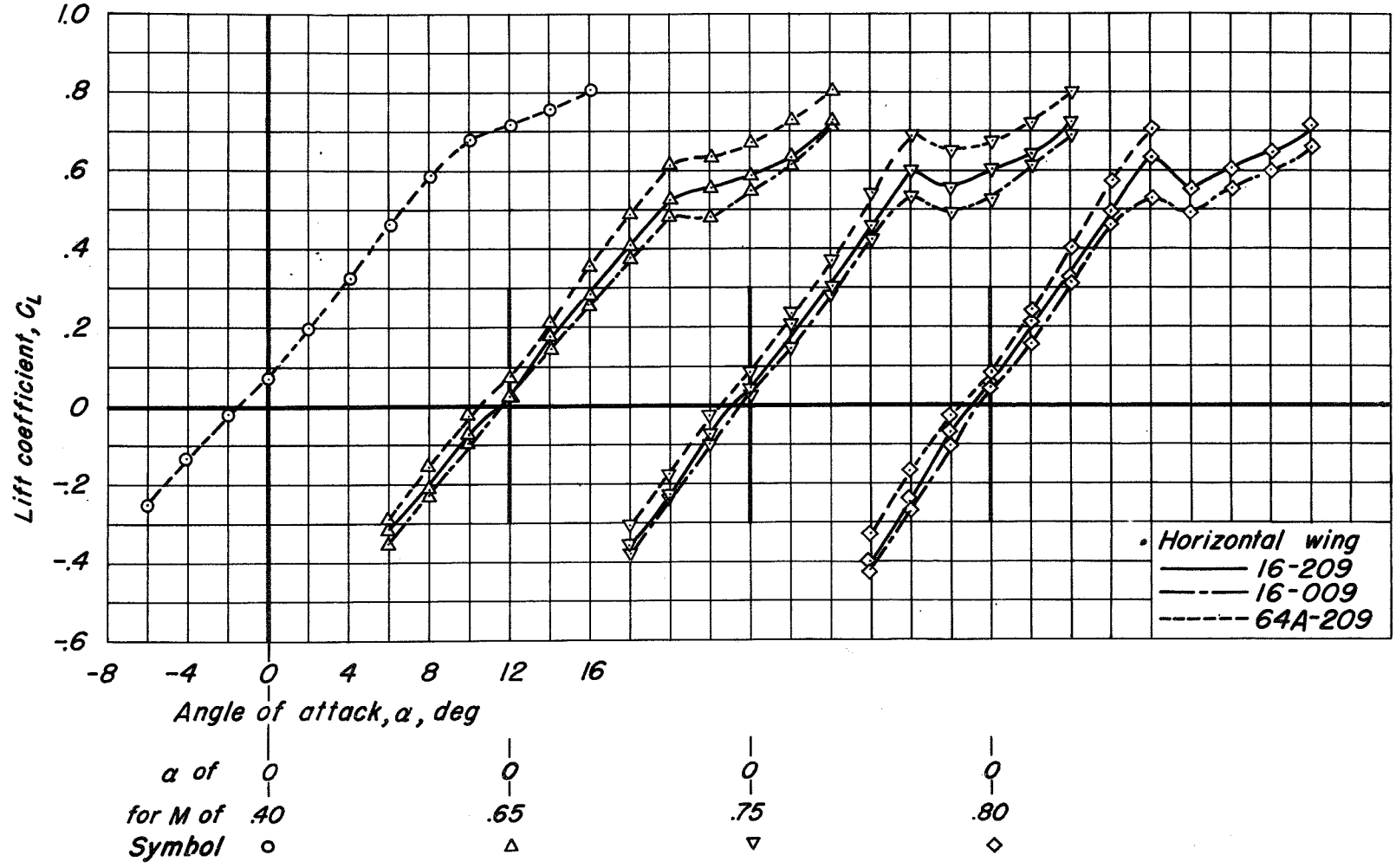

(a) M, 0.40, 0.65, 0.75, 0.80.

Figure 5.- Variation of lift coefficient with angle of attack for the model with three different horizontal wings, less tail. δ_{f_h}, δ_{f_v} = 0°.

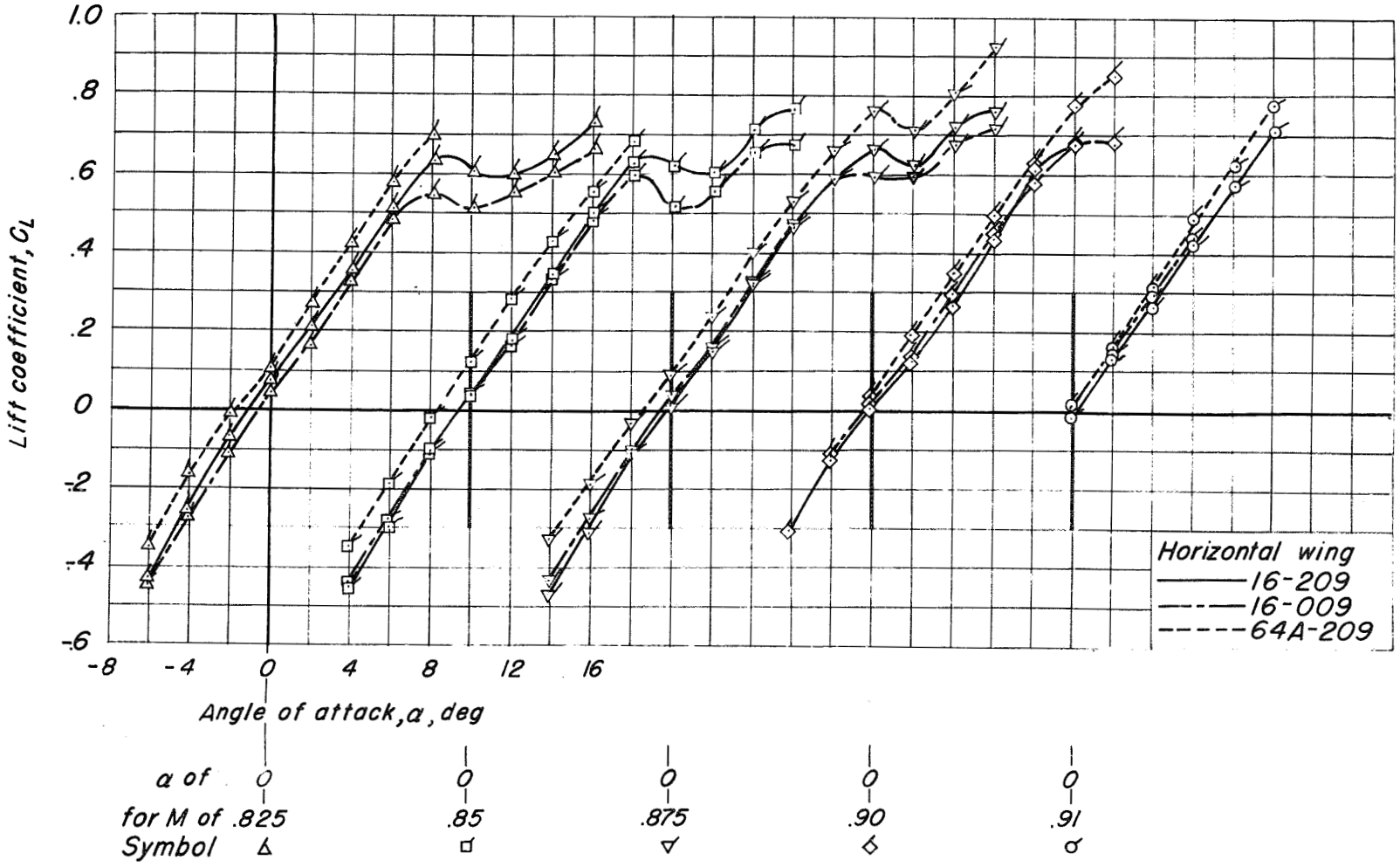

(b) M, 0.825, 0.85, 0.875, 0.90, 0.91.

Figure 5.- Concluded.

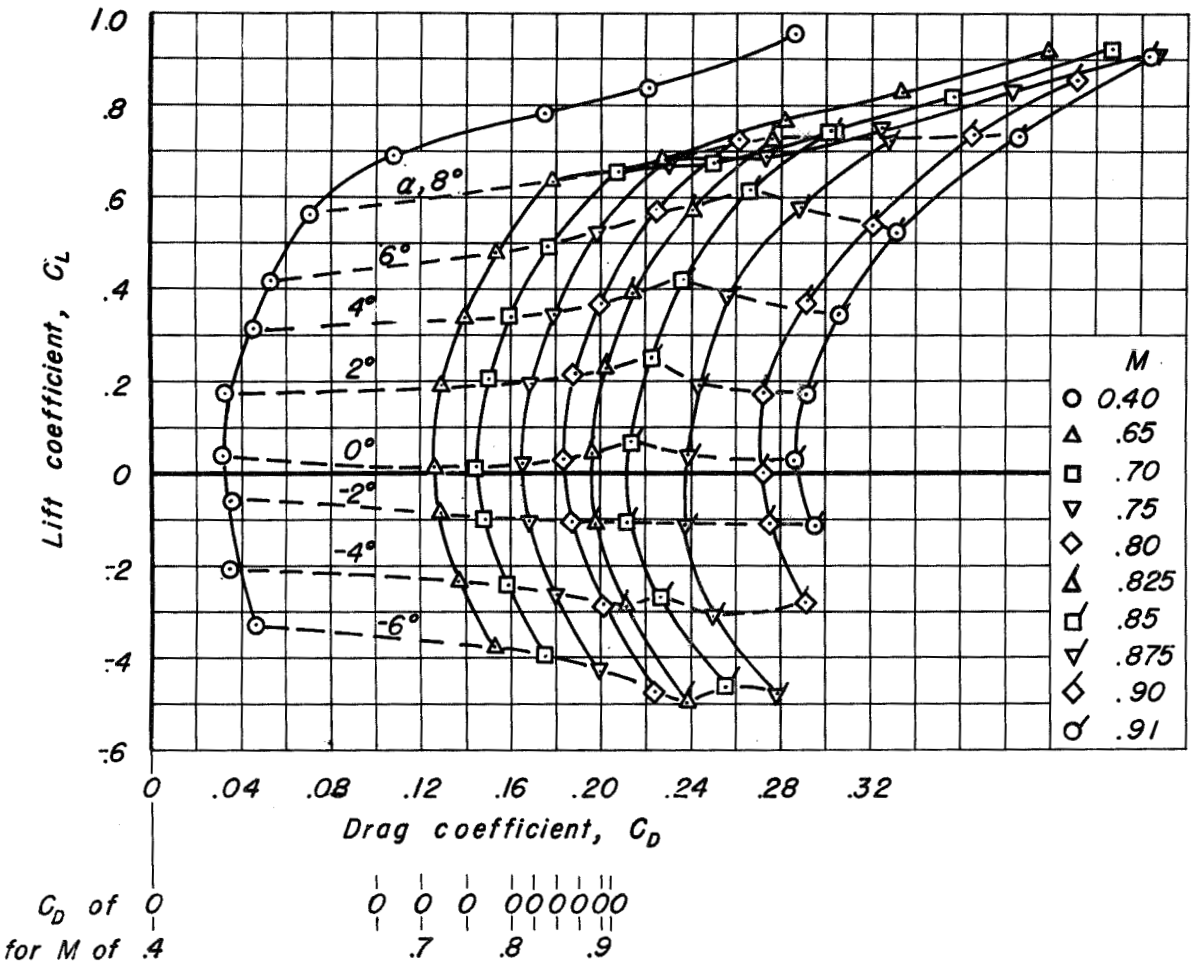

(a) Unrolled.

Figure 6.- Variation of lift coefficient with drag coefficient at various Mach numbers. δ_{f_h}, δ_{f_v}, δ_{f_t}, $i_t = 0°$; W_h, 16-209, W_v, 16-009.

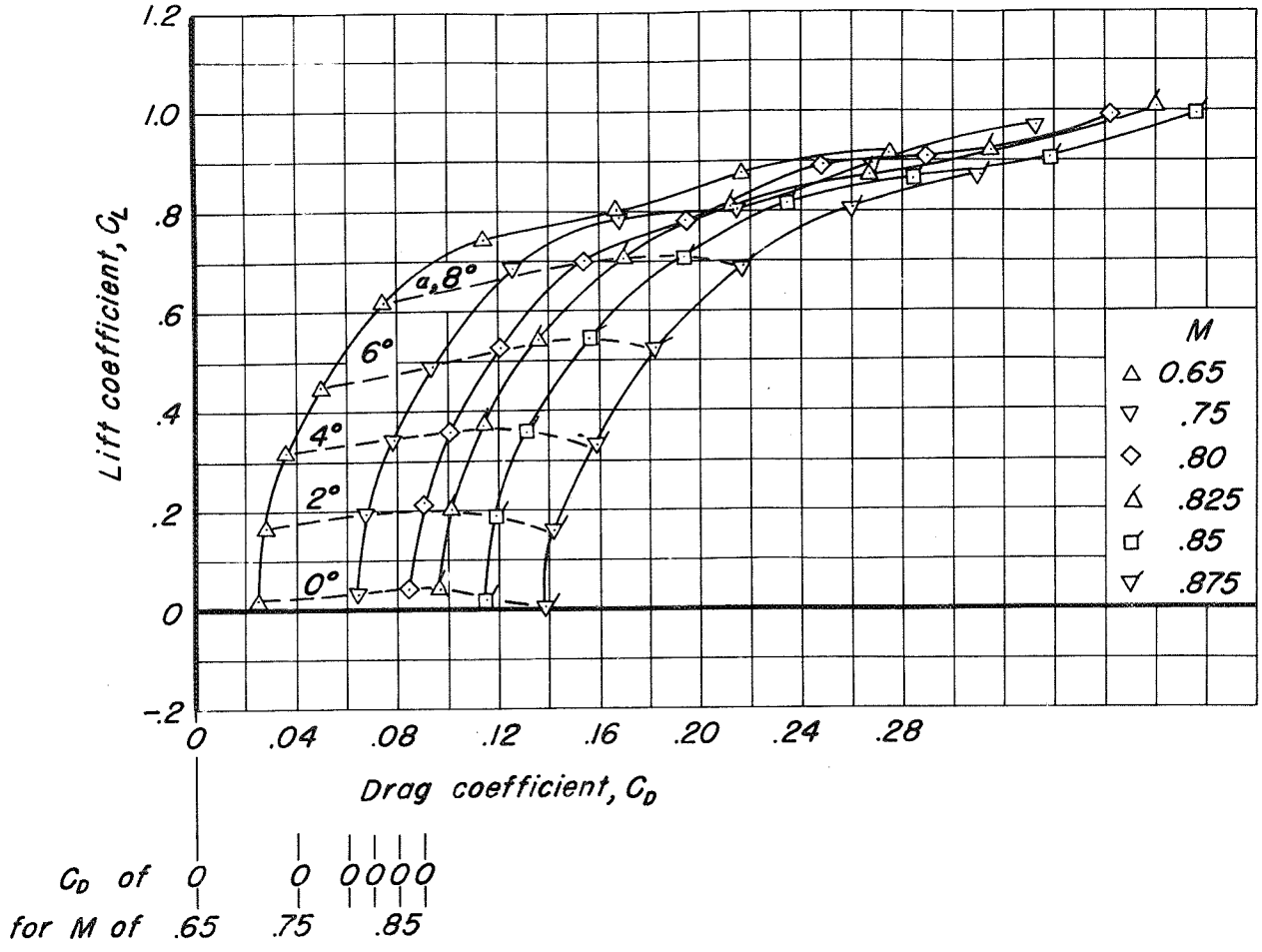

(b) Rolled 22.5°.

Figure 6.- Concluded.

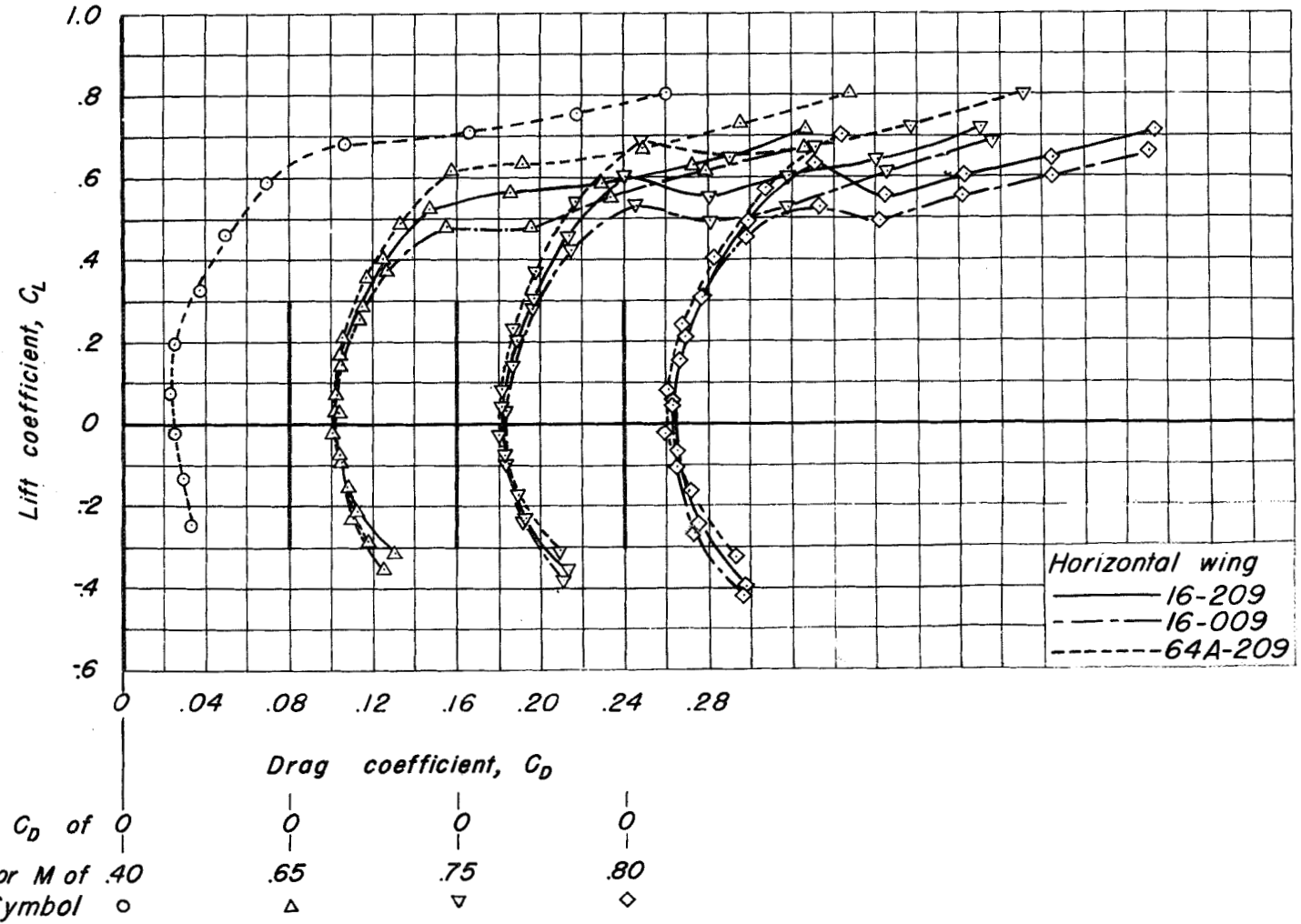

(a) M, 0.40, 0.65, 0.75, 0.80.

Figure 7.— Variation of lift coefficient with drag coefficient for the model with three different horizontal wings, less tail. δ_{f_h}, δ_{f_v} = 0°.

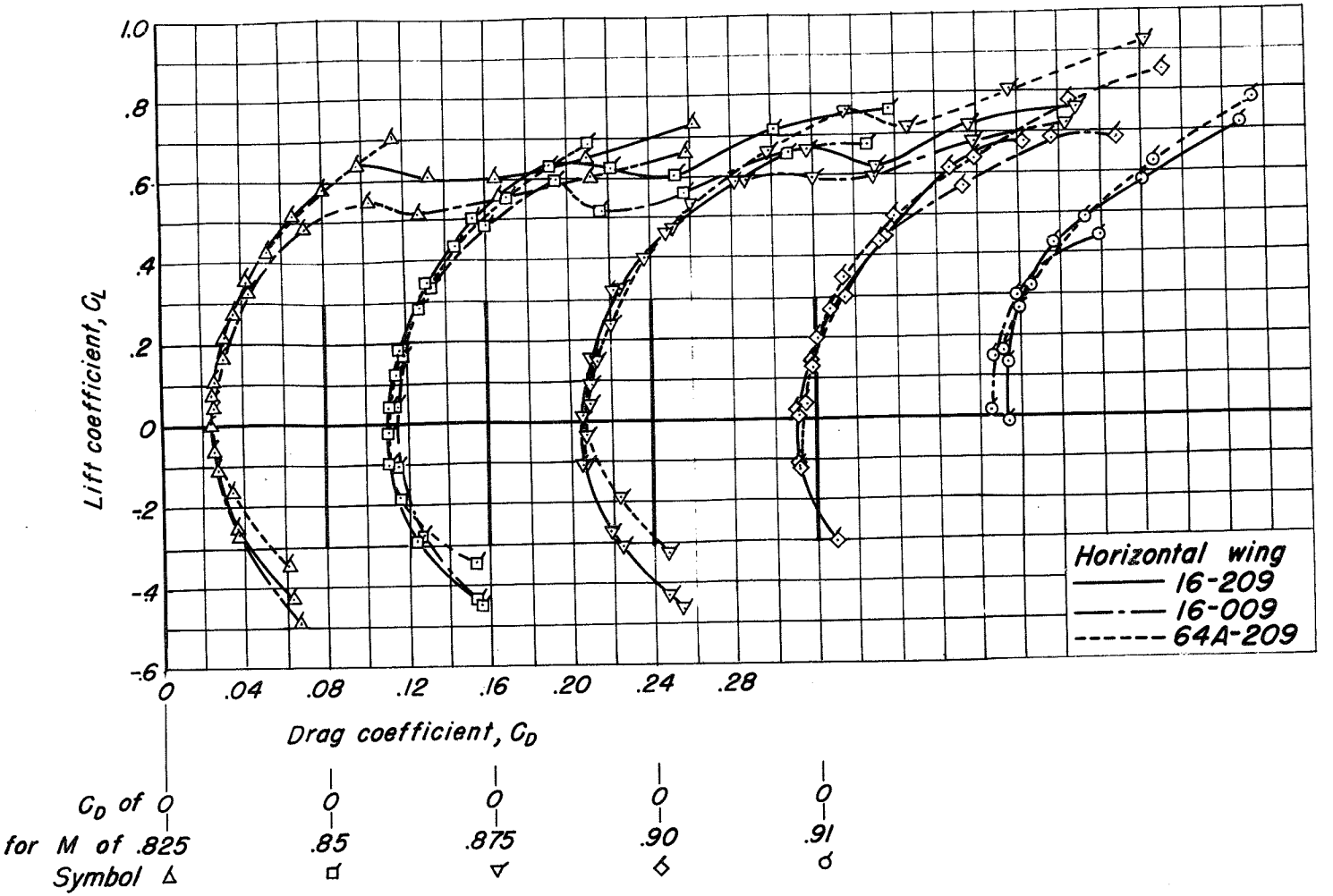

(b) M, 0.825, 0.85, 0.875, 0.90, 0.91.

Figure 7. - Concluded.

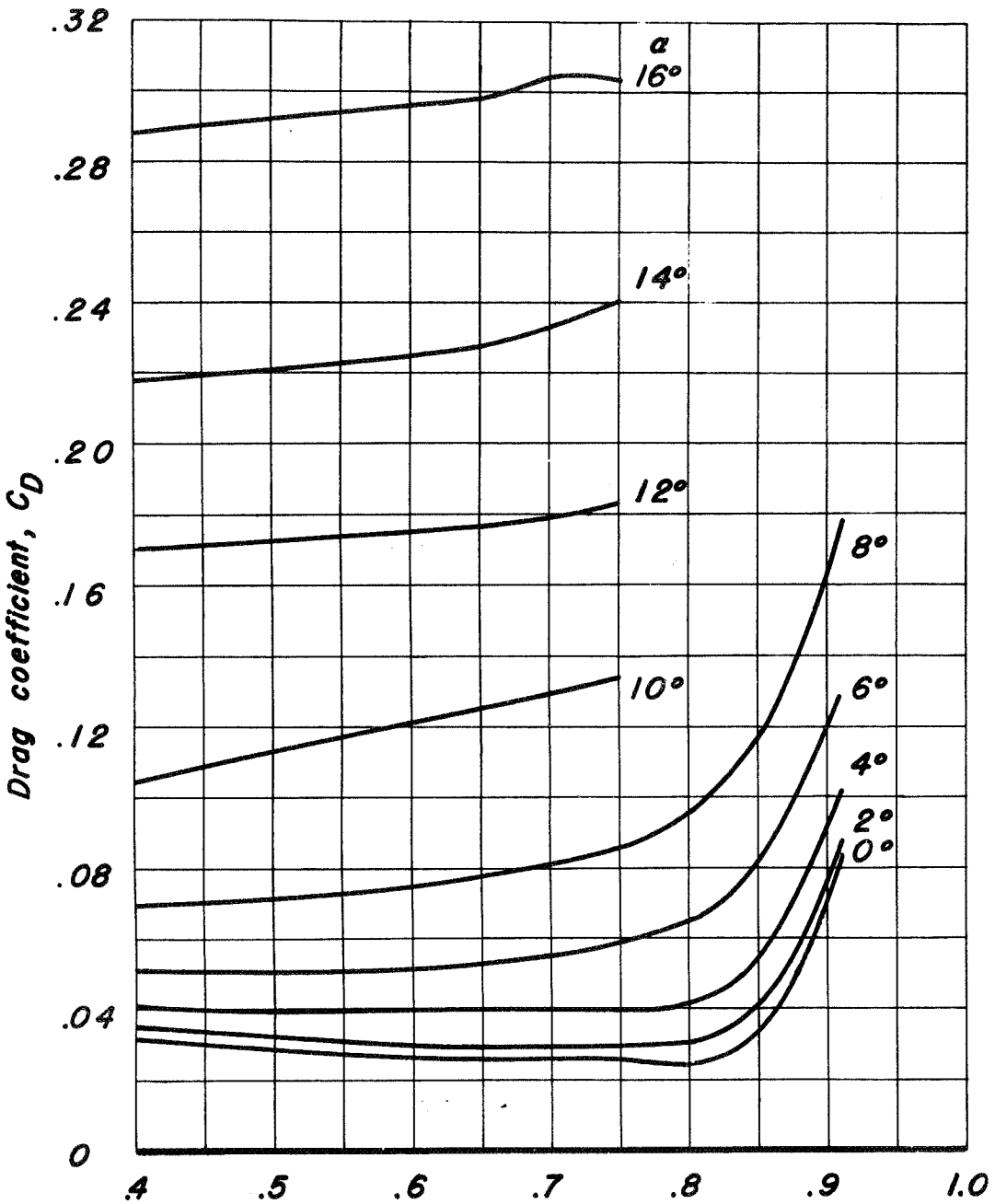

(a) Unrolled.

Figure 8.— Variation of drag coefficient with Mach number at various angles of attack. δ_{t_h}, δ_{f_v}, δ_{f_f}, $i_f = 0°$; W_h, 16-209, W_v, 16-009.

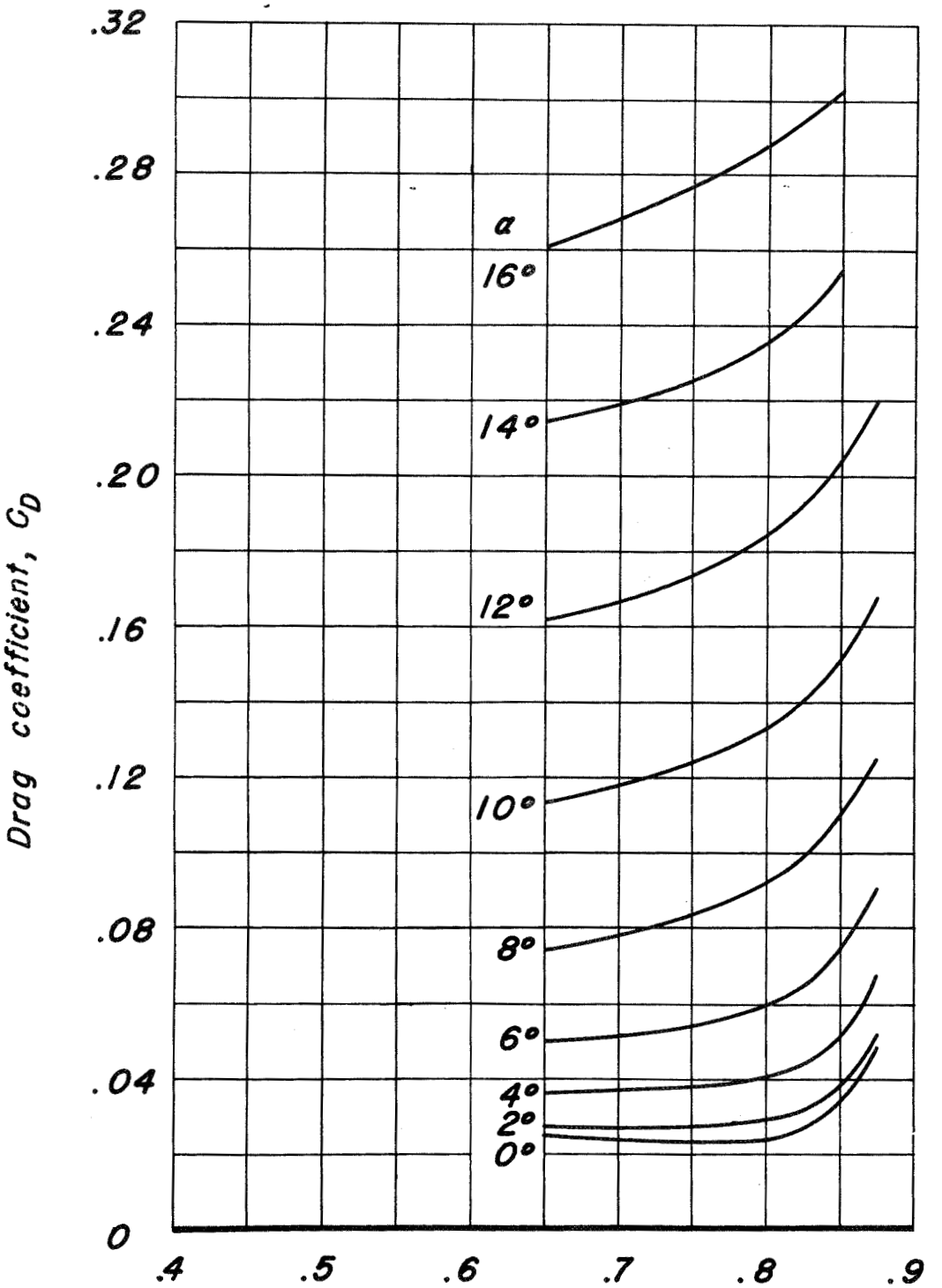

(b) Rolled 22.5°.

Figure 8.— Concluded.

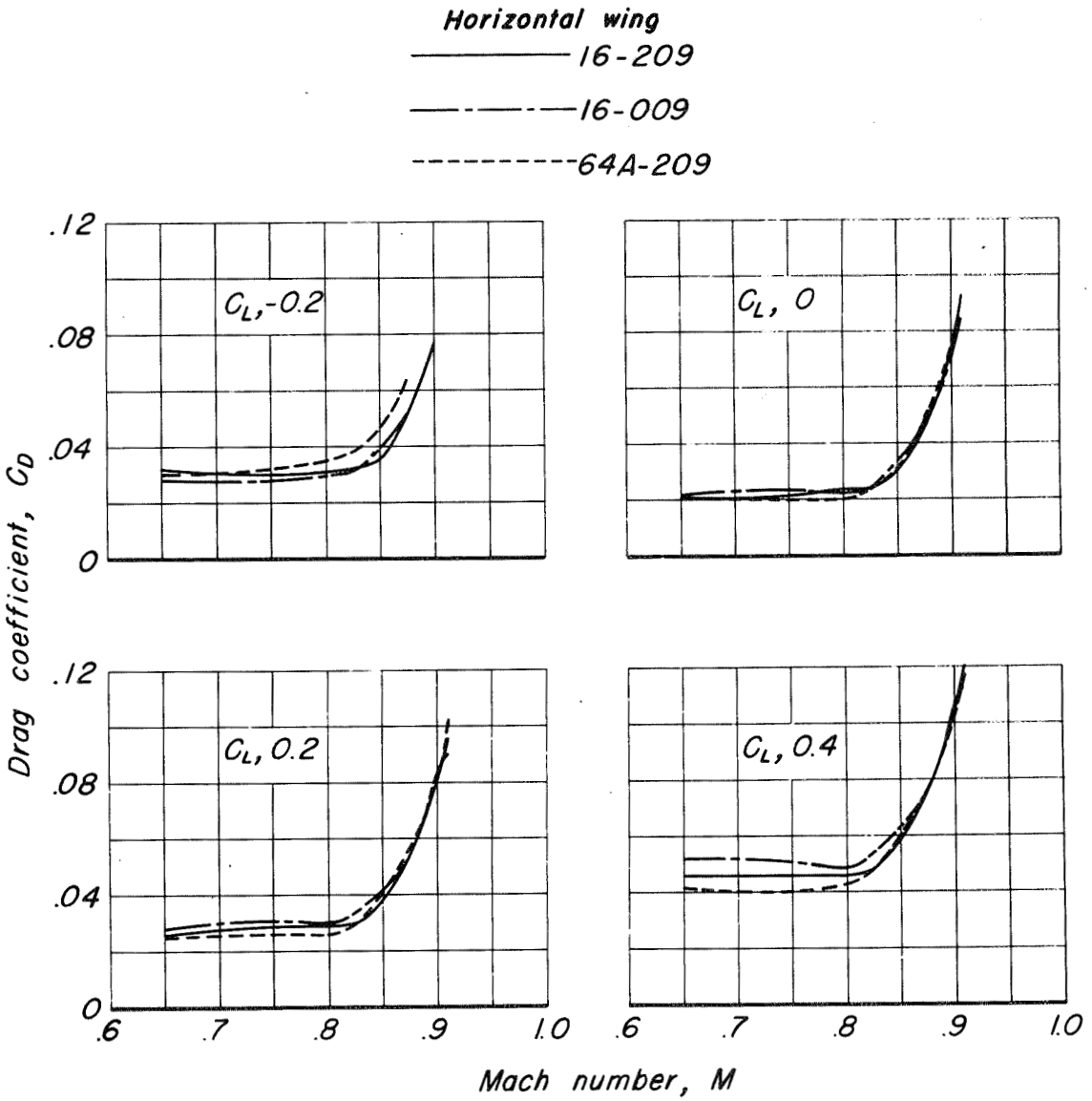

Figure 9.— Variation of drag coefficient with Mach number for the model with three different horizontal wings, less tail. δ_{f_h}, $\delta_{f_v} = 0°$.

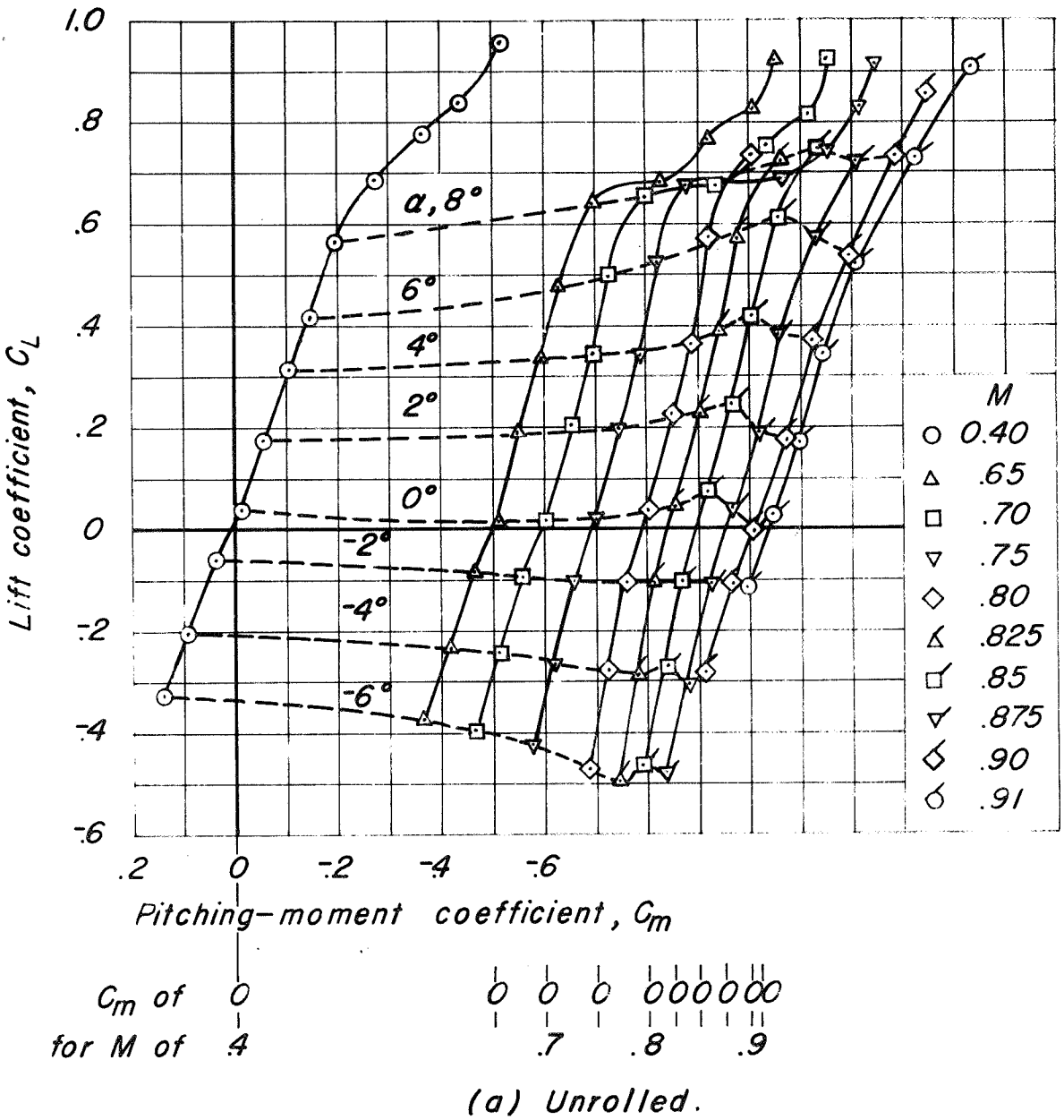

(a) Unrolled.

Figure 10.— Variation of lift coefficient with pitching-moment coefficient. δ_{f_h}, δ_{f_v}, δ_{f_t}, $i_t = 0°$; W_h, 16-209, W_v, 16-009.

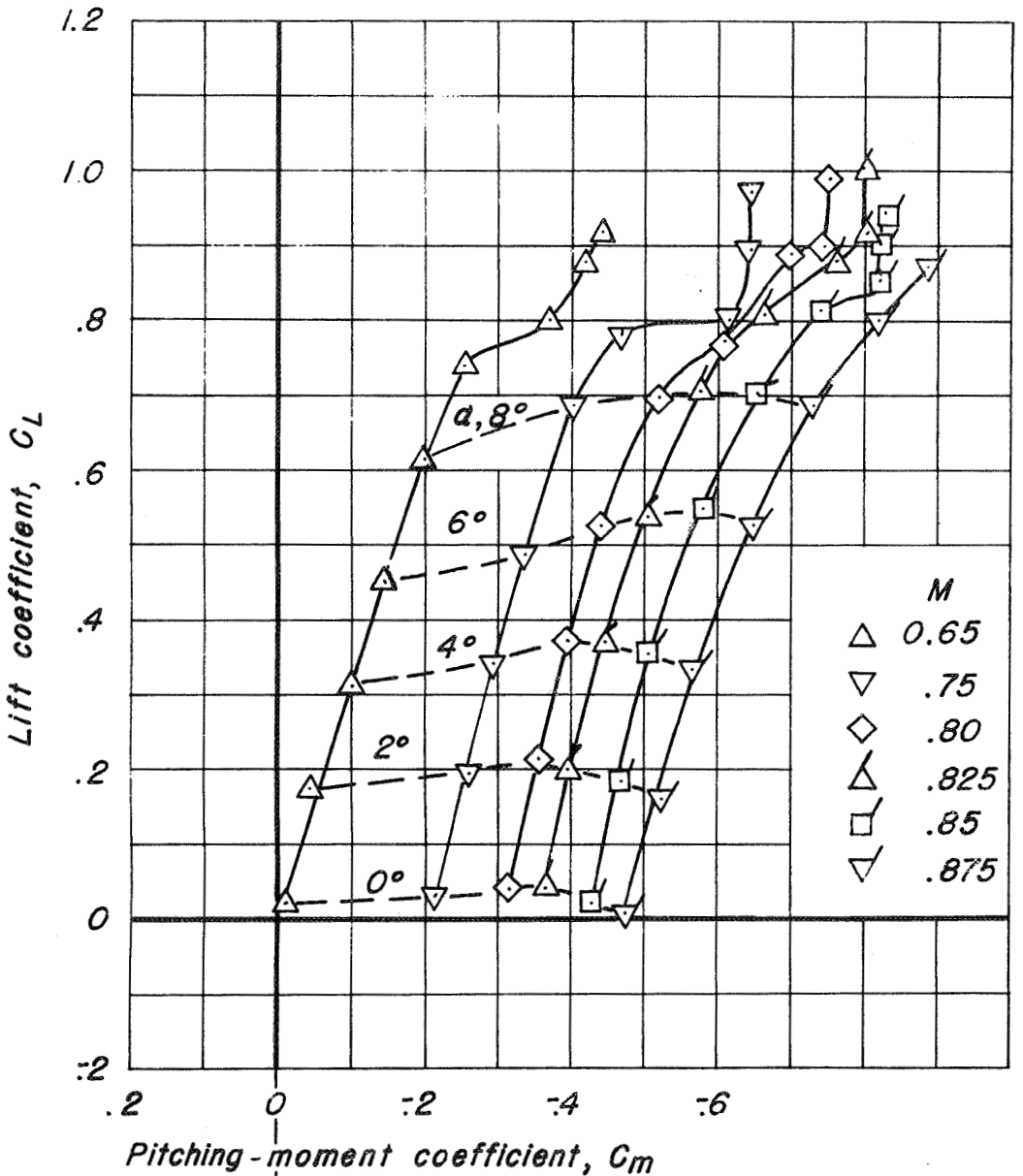

(b) Rolled 22.5°.

Figure 10.— Concluded.

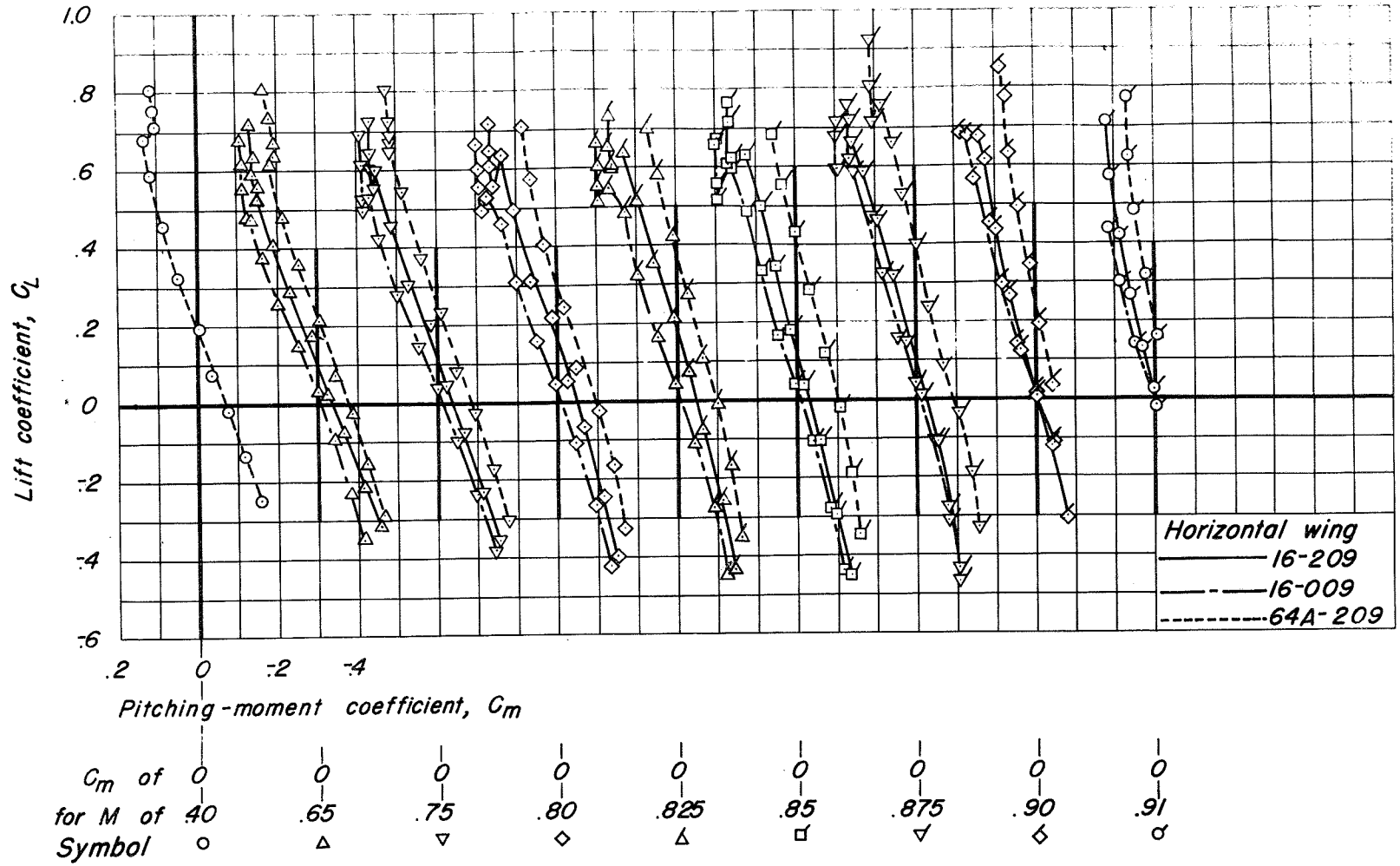

Figure 11.- Variation of lift coefficient with pitching-moment coefficient for the model with three different horizontal wings, less tail. δ_{f_h}, δ_{f_v} = 0°.

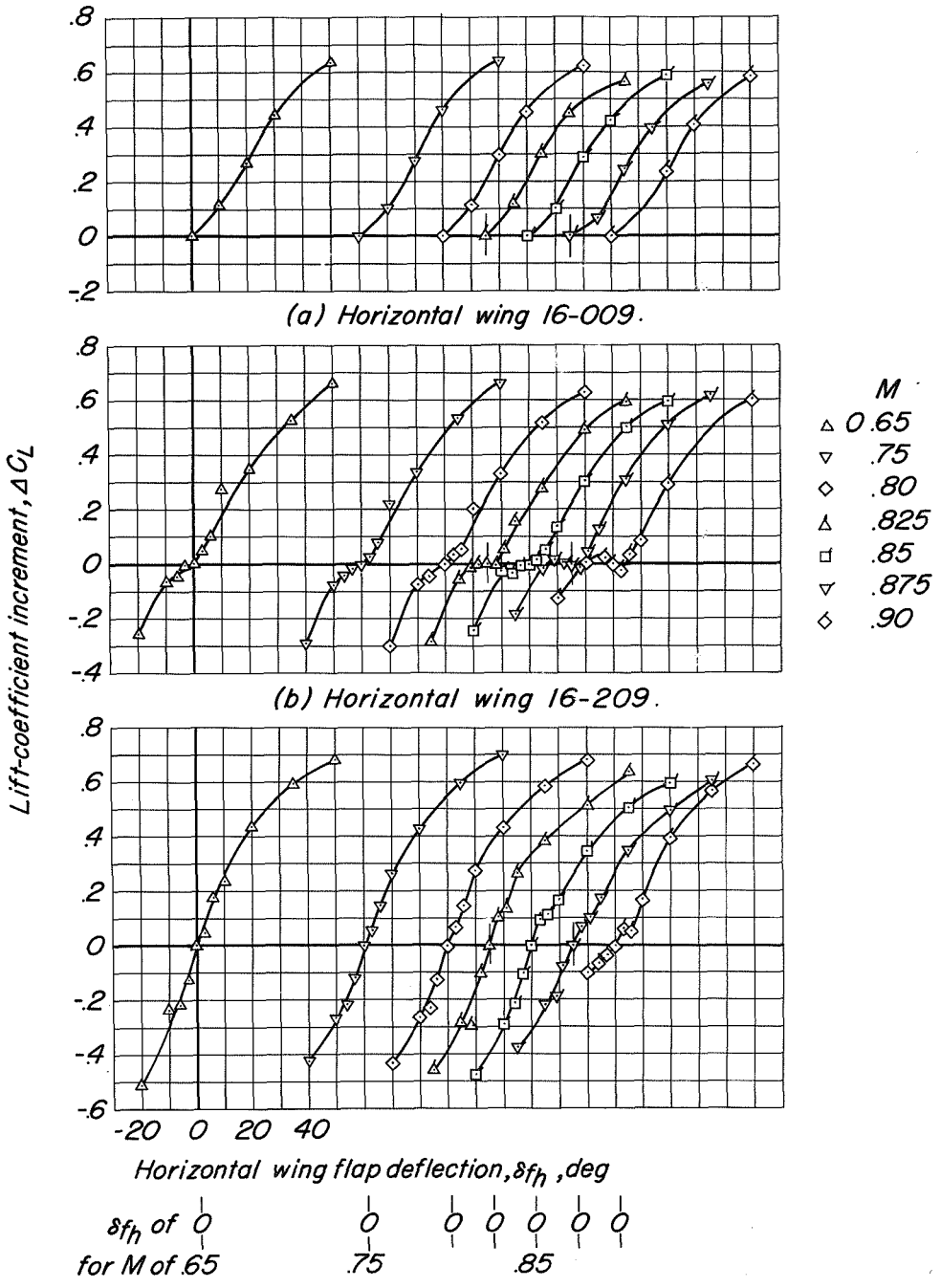

Figure 12.— Variation of lift-coefficient increment with horizontal flap deflection for three different horizontial wings, model less tail. α, $\delta_{f_V} = 0°$

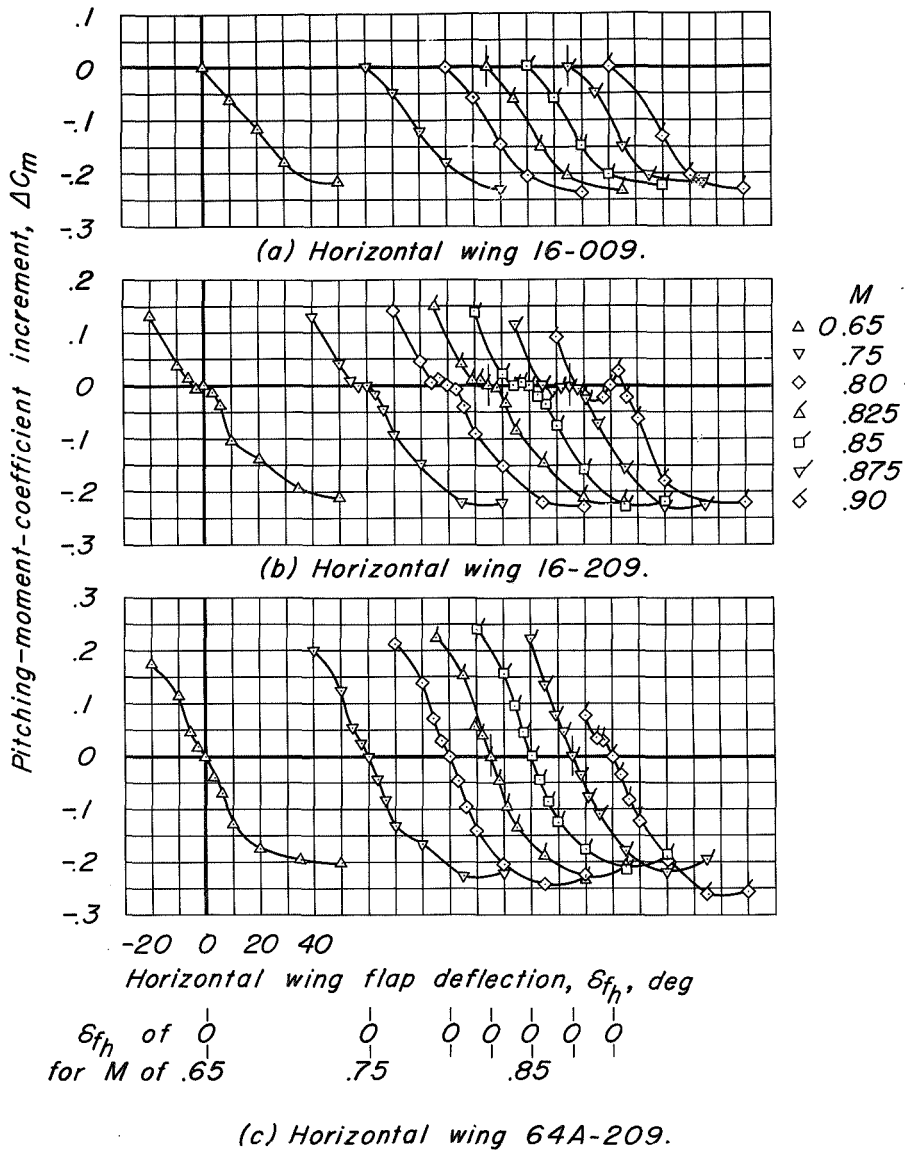

(c) Horizontal wing 64A-209.

Figure 13.—Variation of pitching-moment-coefficient increment with horizontal wing flap deflection for three different horizontal wings, model less tail. $\alpha, \delta_{f_v}=0°$.

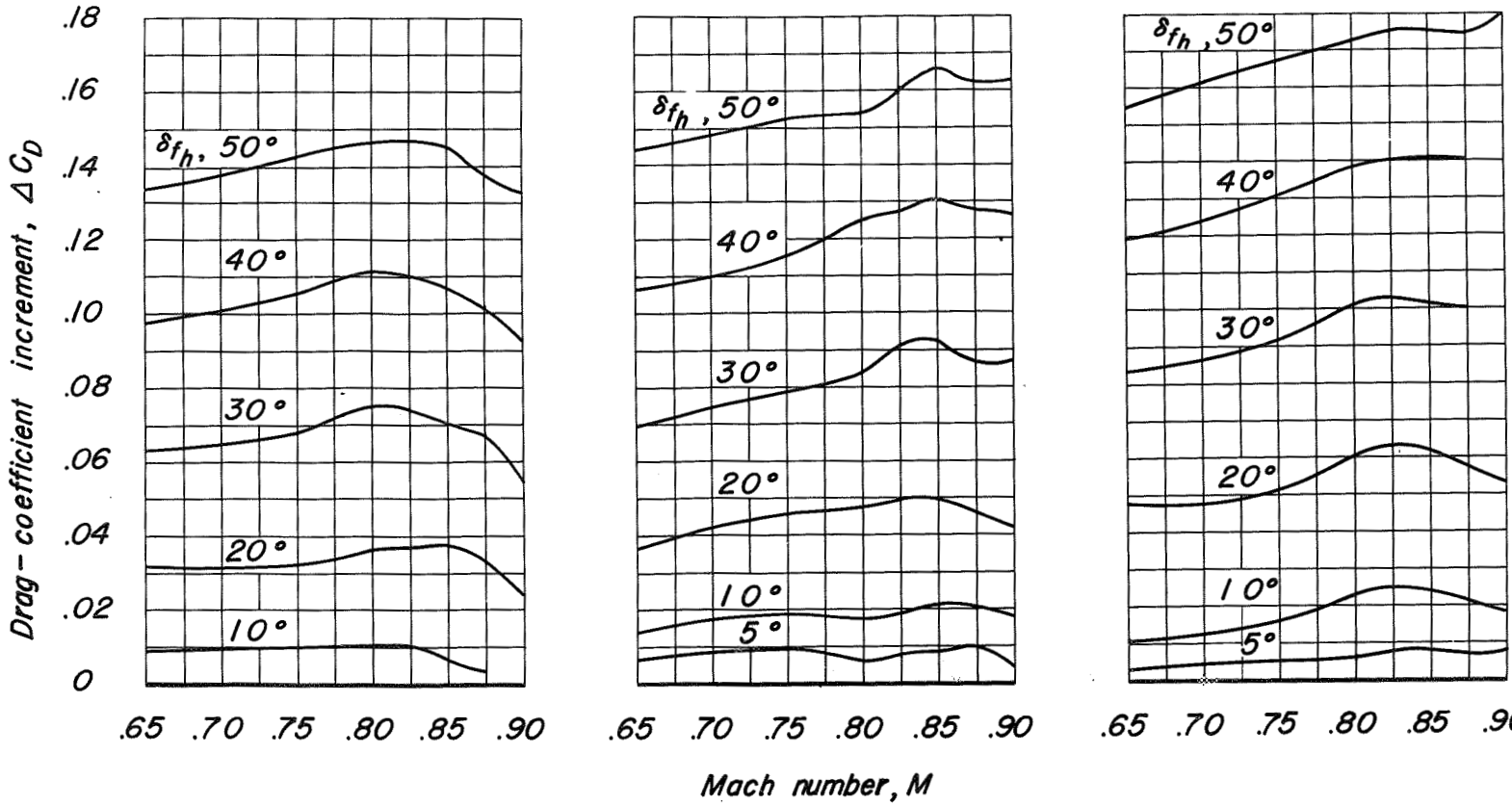

(a) Horizontal wing 16-009. (b) Horizontal wing 16-209. (c) Horizontal wing 64A-209.

Figure 14.—Variation of drag-coefficient increment with Mach number due to horizontal flap defections for three different horizontal wings, model less tail. α, δ_{f_v}=0°.

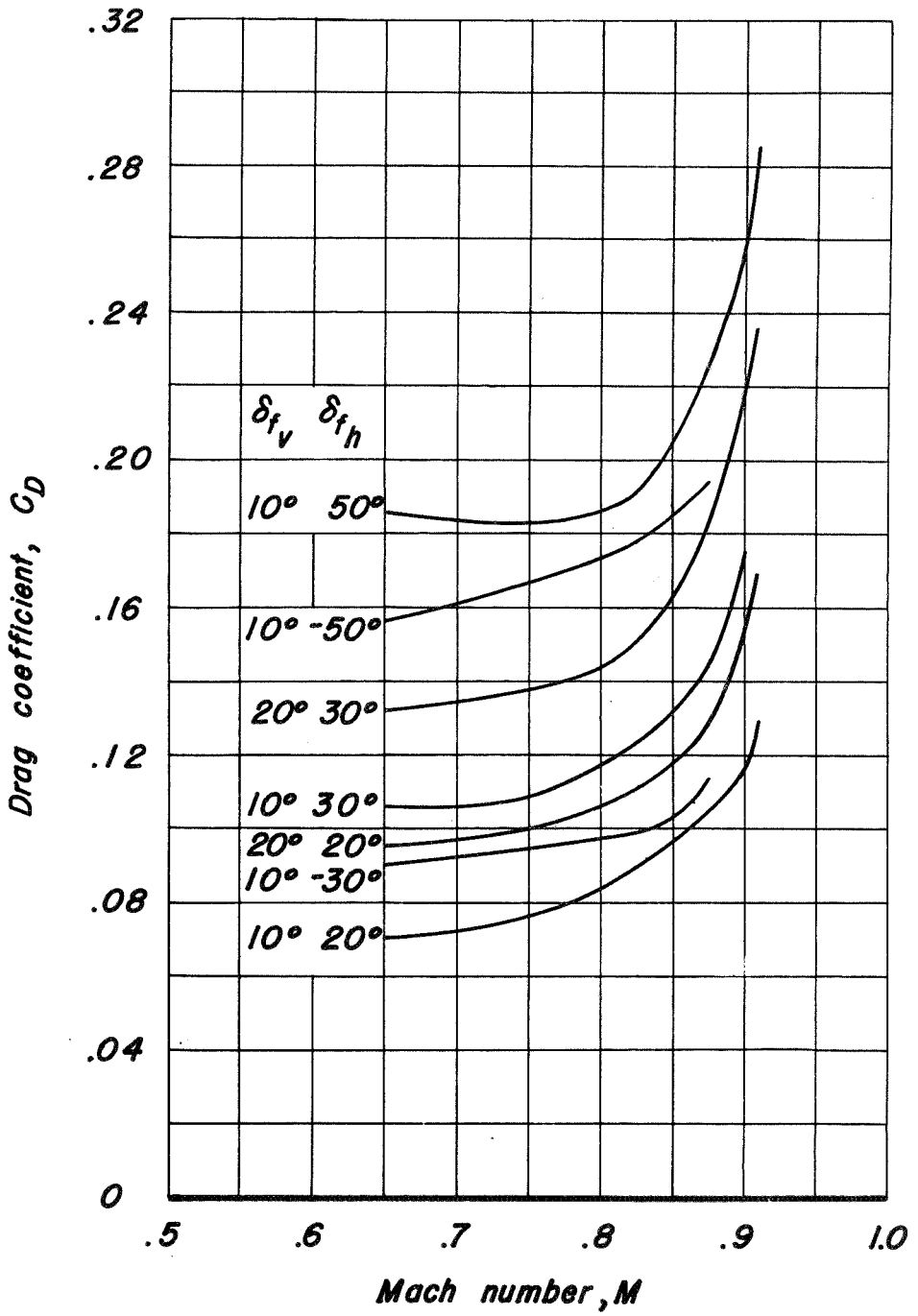

Figure 15.—Variation with Mach number of drag coefficient for various combinations of horizontal and vertical flap deflections. α, δ_{f_t}, $i_t = 0°$; W_h, 16-209, W_v, 16-009.

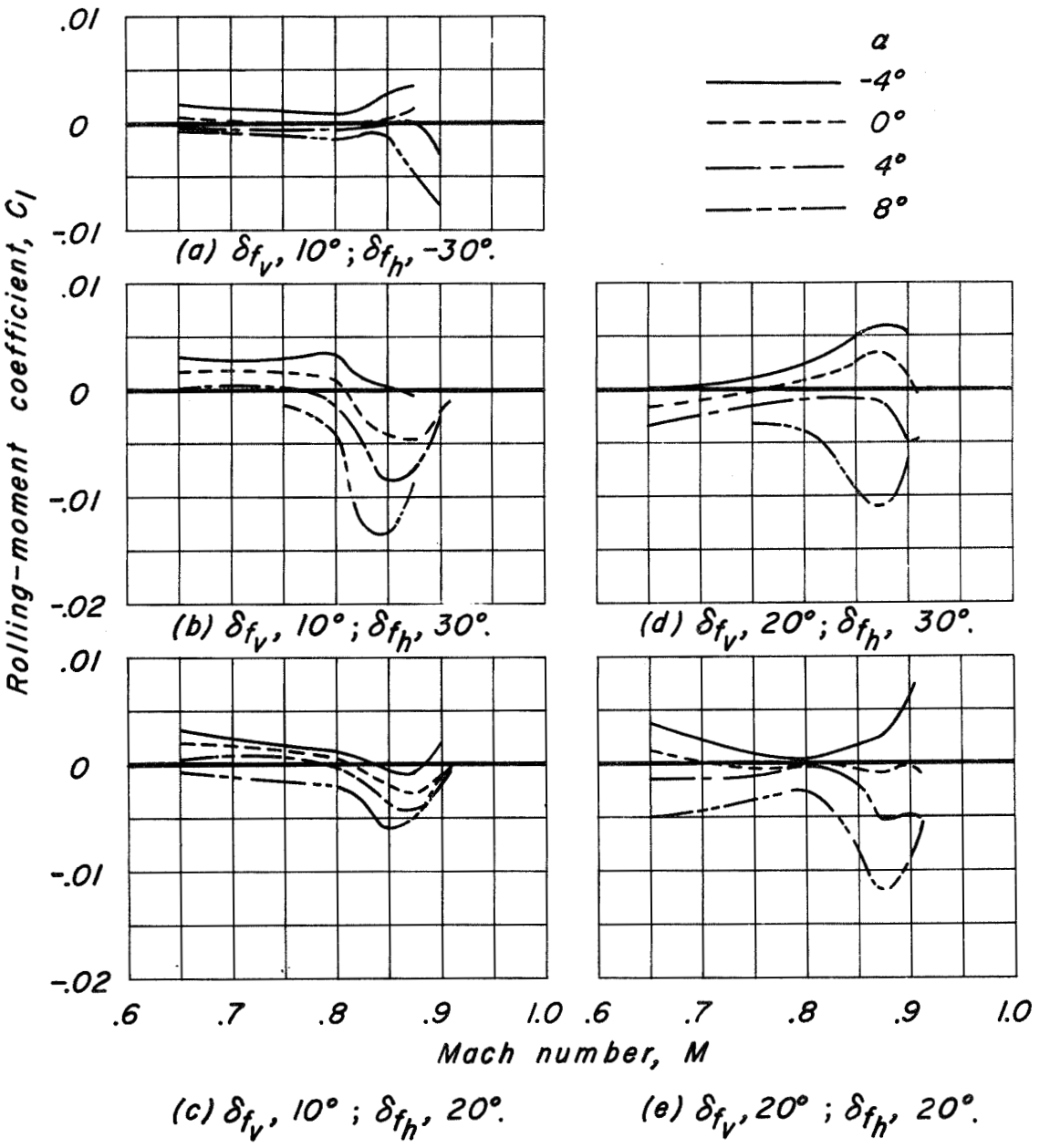

Figure 16.- Variation of rolling-moment coefficient with Mach number for various angles of attack with various combinations of horizontal and vertical flap deflections. δ_{f_t}, i_t = 0°; W_h, 16-209, W_v, 16-009.

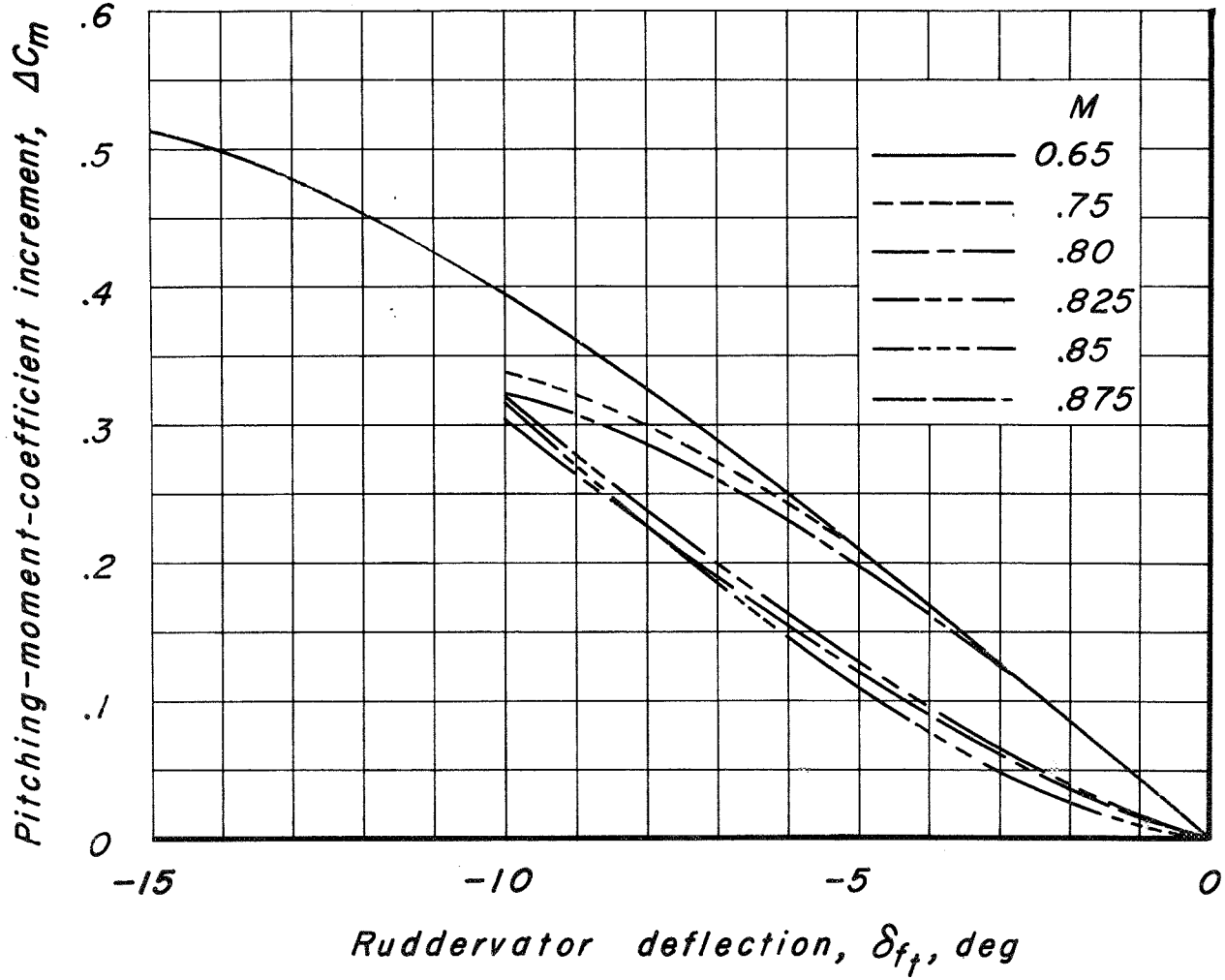

Figure 17.— Pitching - moment - coefficient increments due to ruddervator deflections at various Mach numbers. α, δ_{f_h}, δ_{f_v}, $i_t = 0°$; W_h, 16-209, W_v, 16-009.

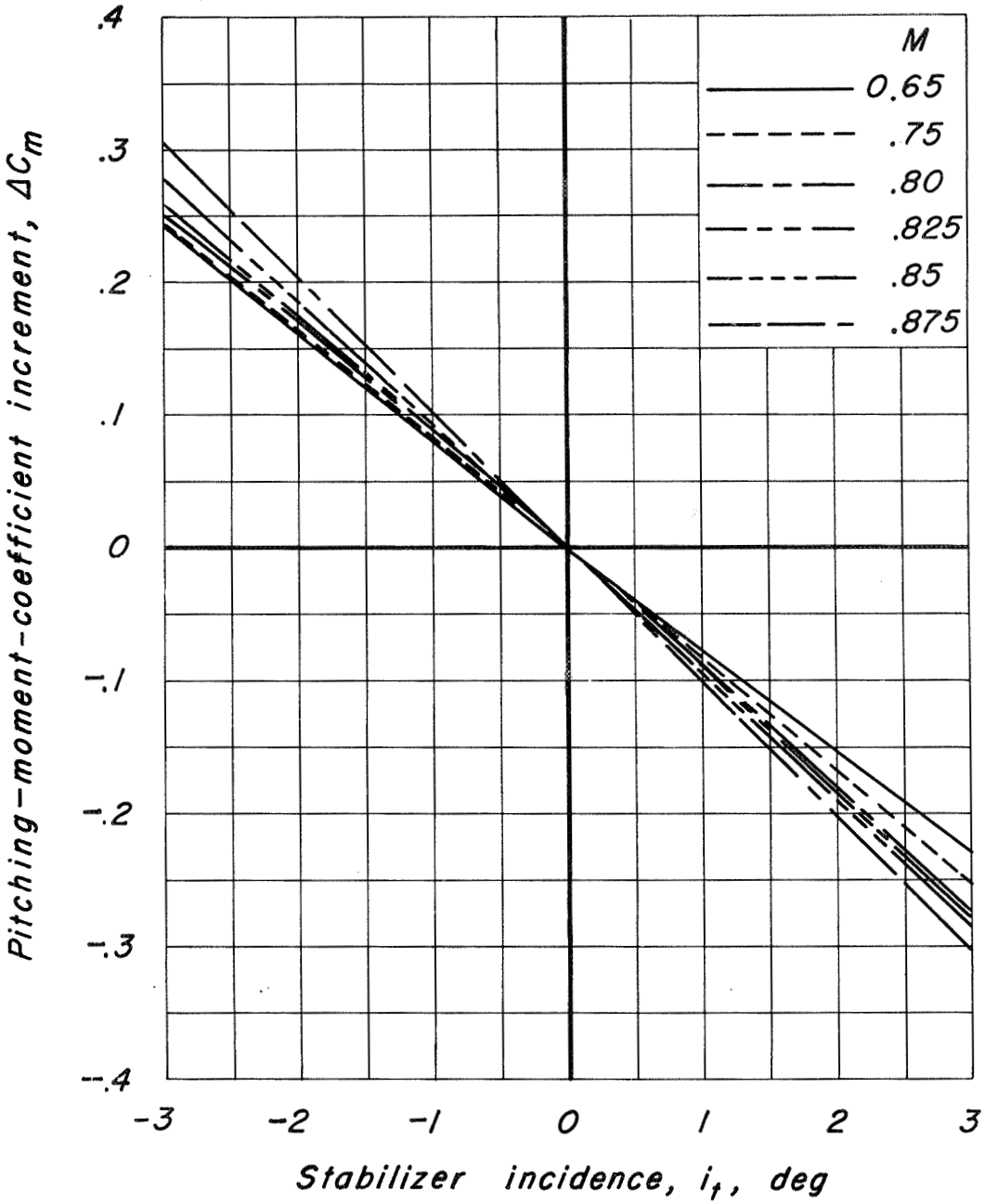

Figure 18.- Pitching-moment-coefficient increments due to tail-incidence variation at various Mach numbers. α, δ_{f_h}, δ_{f_v}, $\delta_{f_t} = 0°$; W_h, 16-209, W_v, 16-009.

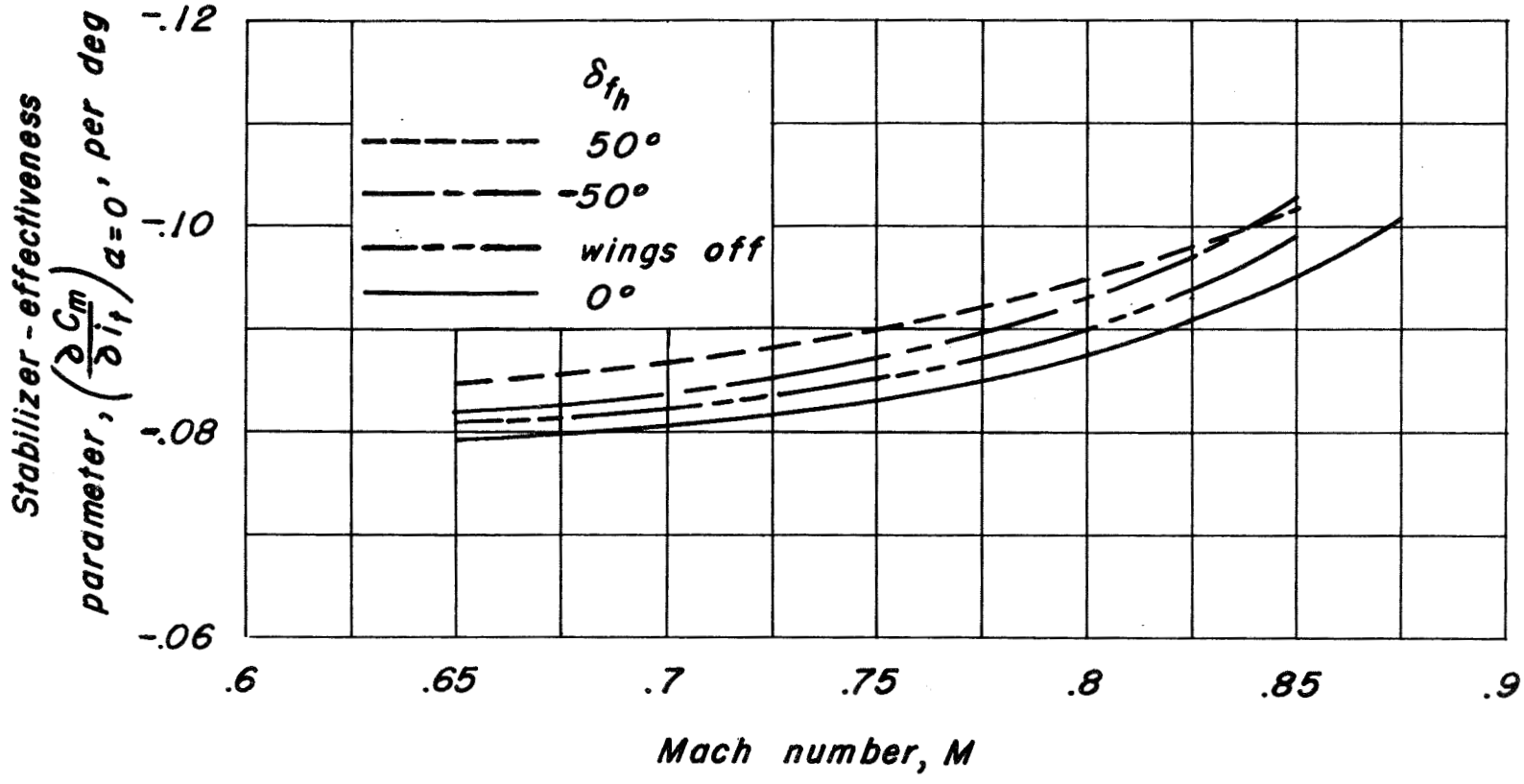

Figure 19.— Variation of stabilizer effectiveness with Mach number for several wing flap deflections and with the wings off. a, δ_{f_f}, $\delta_{f_v} = 0°$, W_h, 16-209, W_v, 16-009.

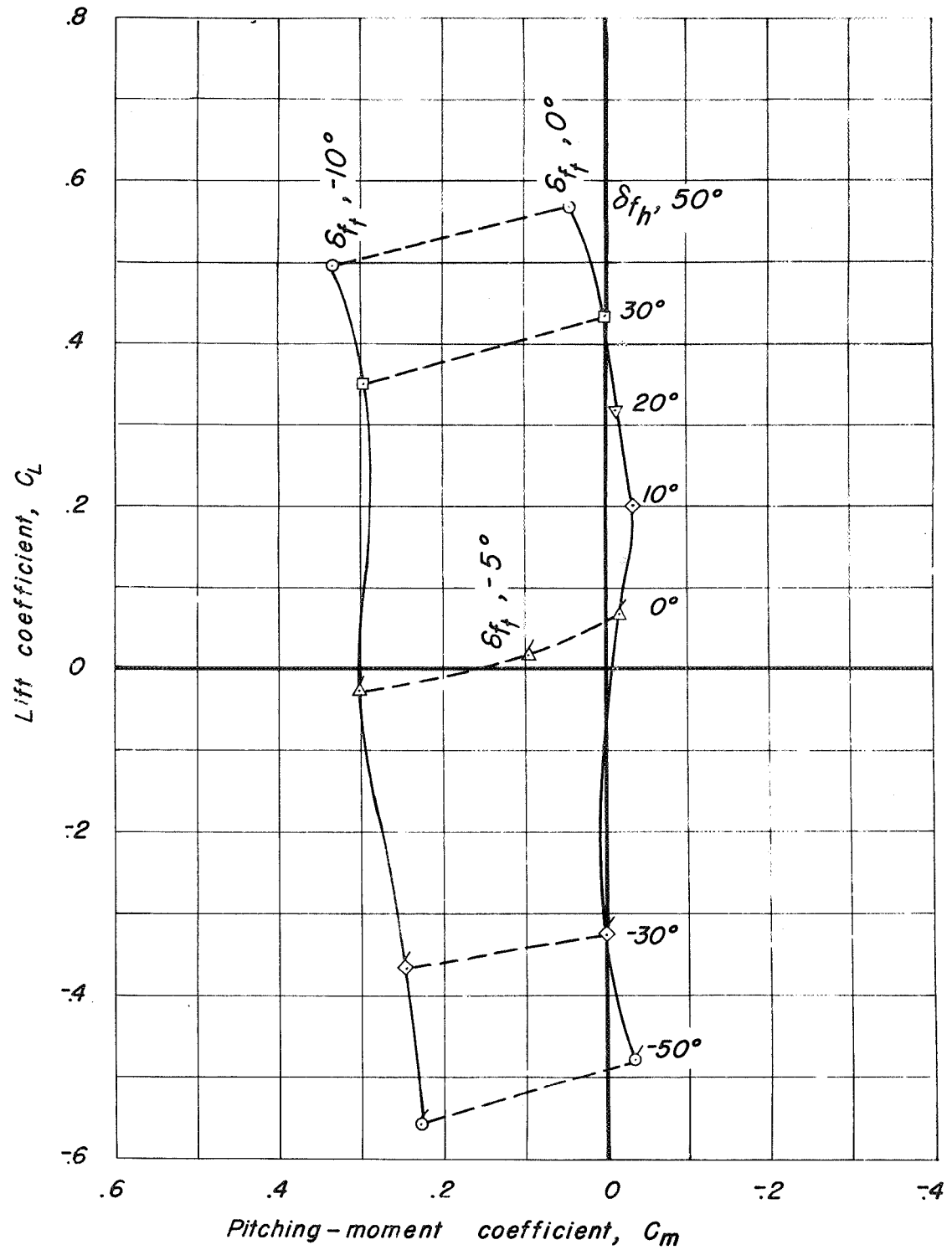

Figure 20.- Variation of pitching-moment coefficient with lift coefficient for various deflections of horizontal wing flaps and ruddervators at a Mach number of 0.85. α, δ_{f_v}, $i_t = 0°$; W_h, 16-209, W_v, 16-009.

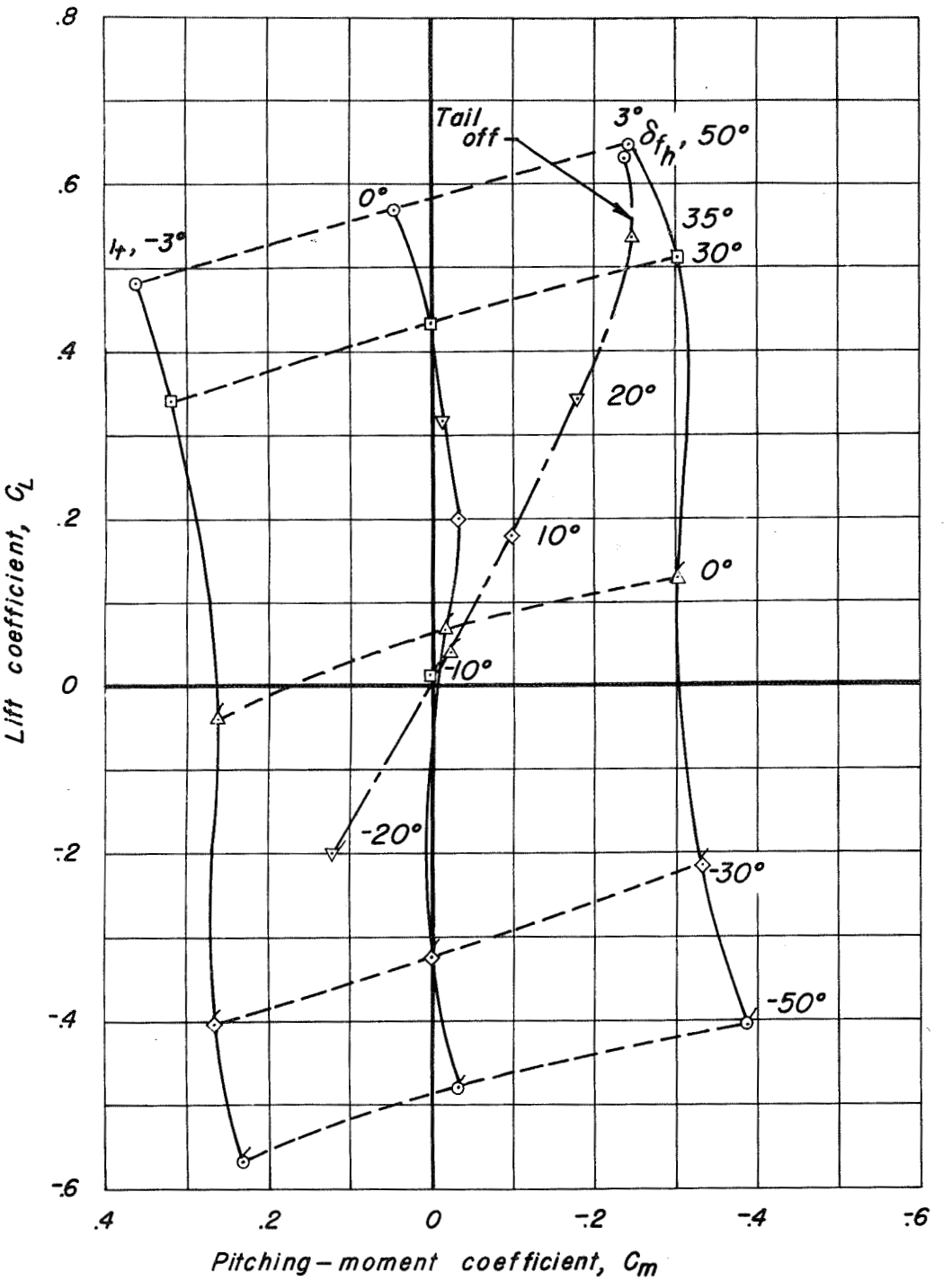

Figure 21.- Variation of pitching-moment coefficient with lift coefficient for various tail incidences and horizontal wing flap deflections at a Mach number of 0.85, with and without tail. α, δ_{f_v}, δ_{f_t} = 0°; W_h, 16-209, W_v, 16-009.

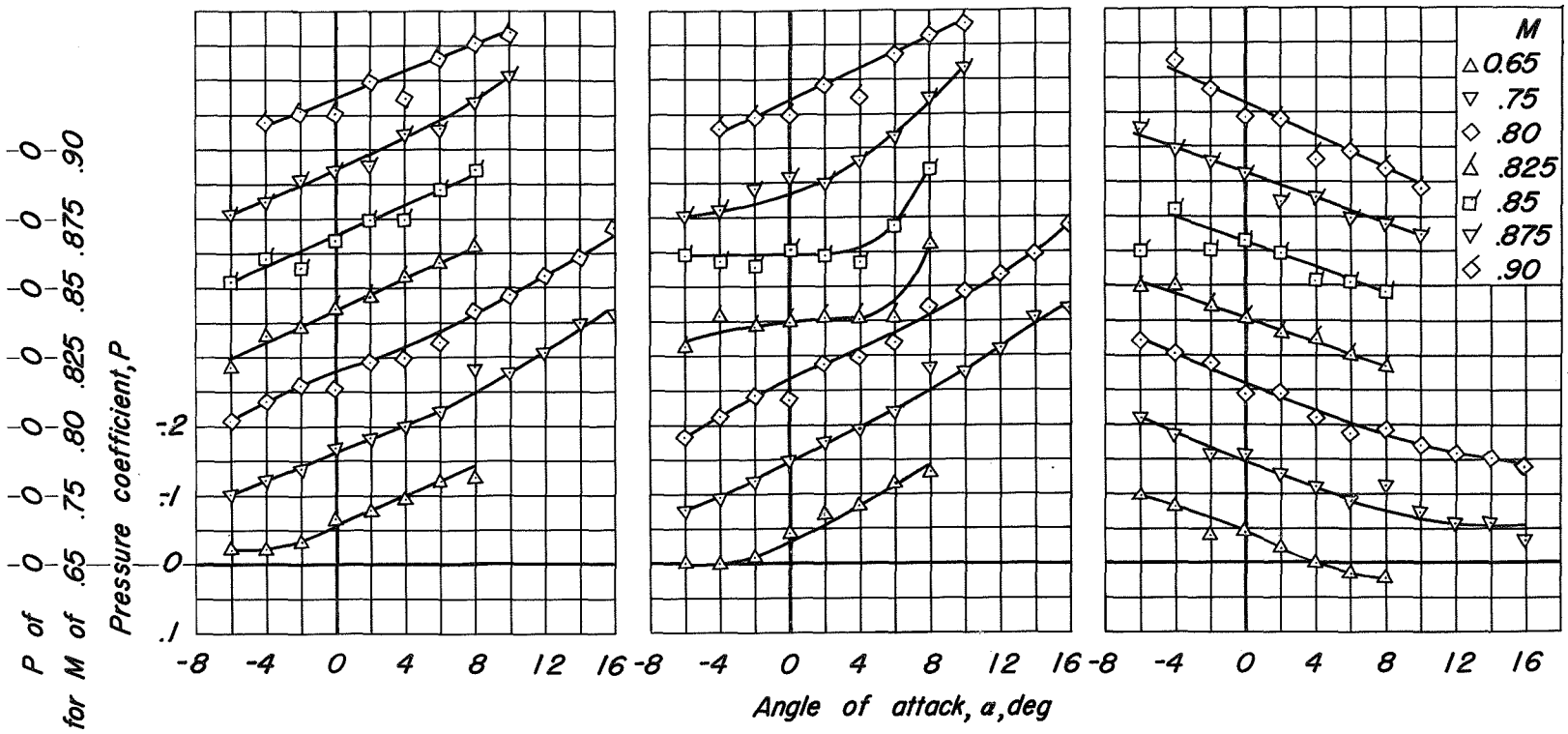

(a) Orifice A. (b) Orifice B. (c) Orifice C.

Figure 22.— Variation of pressure coefficient with angle of attack at various nose orifices of the normal nose. Orifices 45° to vertical plane as shown in figure 2(a).

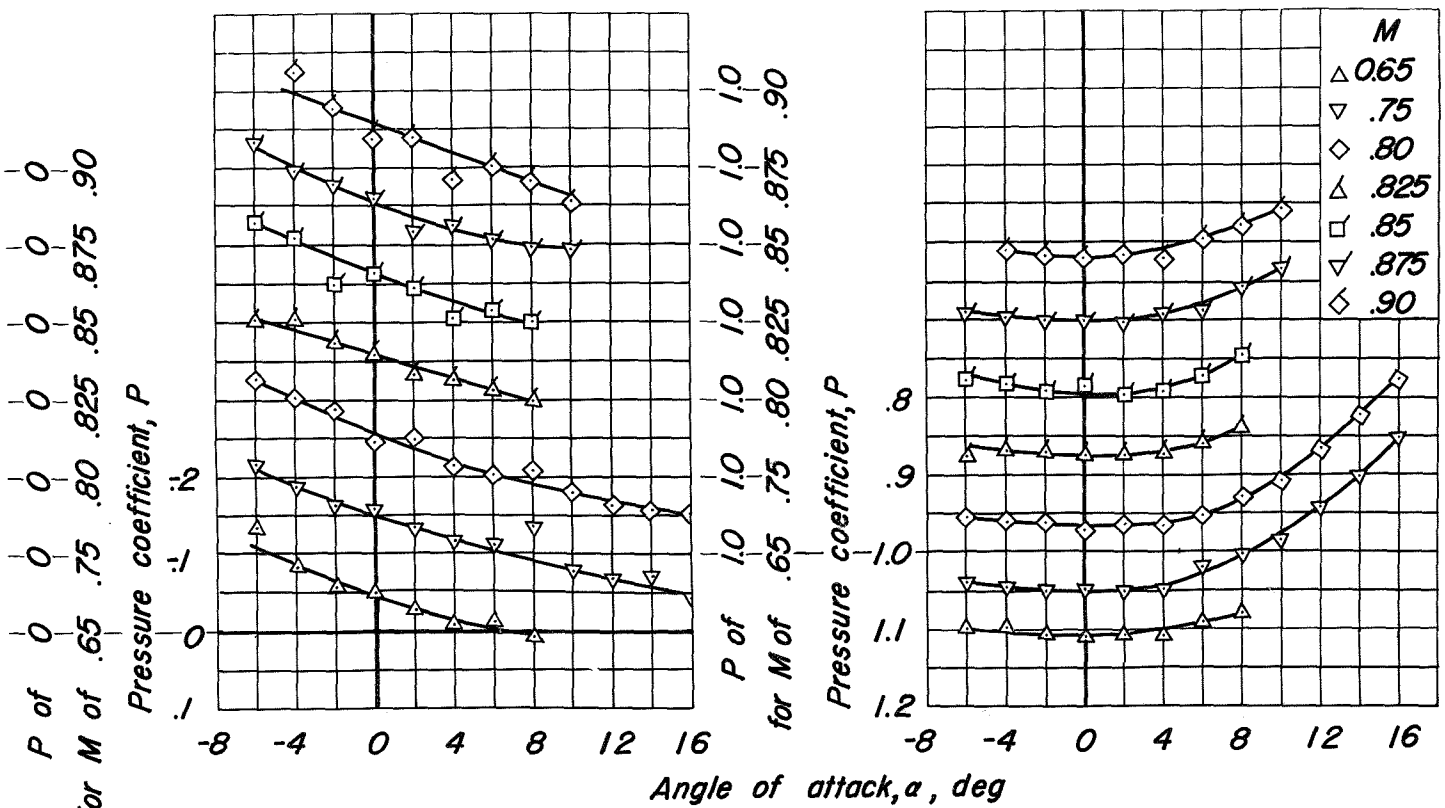

(d) Orifice D.

(e) Orifice E.

Figure 22.— Concluded.

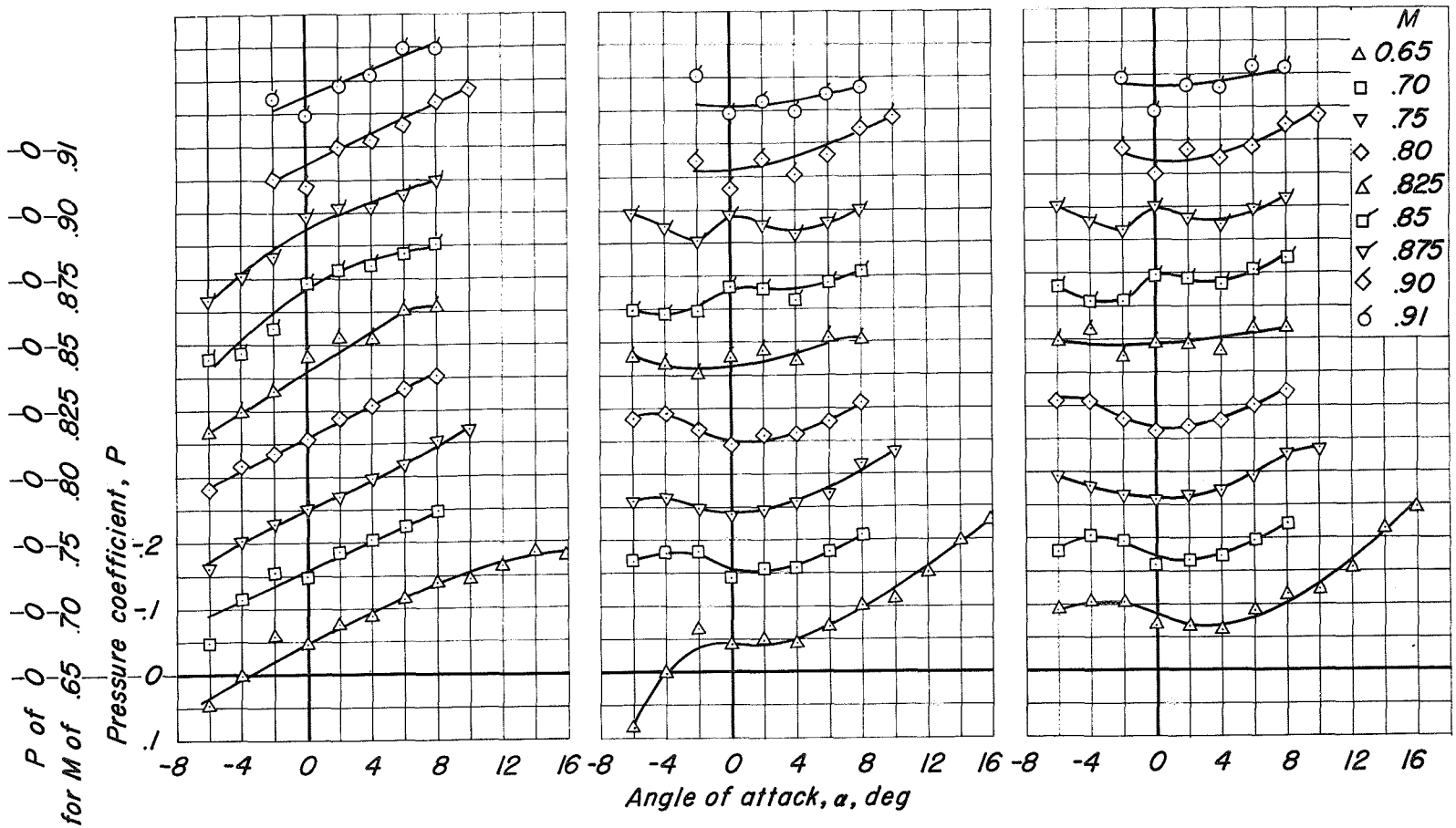

(a) Orifice A'. (b) Orifice B'. (c) Orifice D'.

Figure 23.— Variation of pressure coefficient with angle of attack at various nose orifices of the normal nose. Orifices in horizontal and vertical planes as shown in figure 2(b).

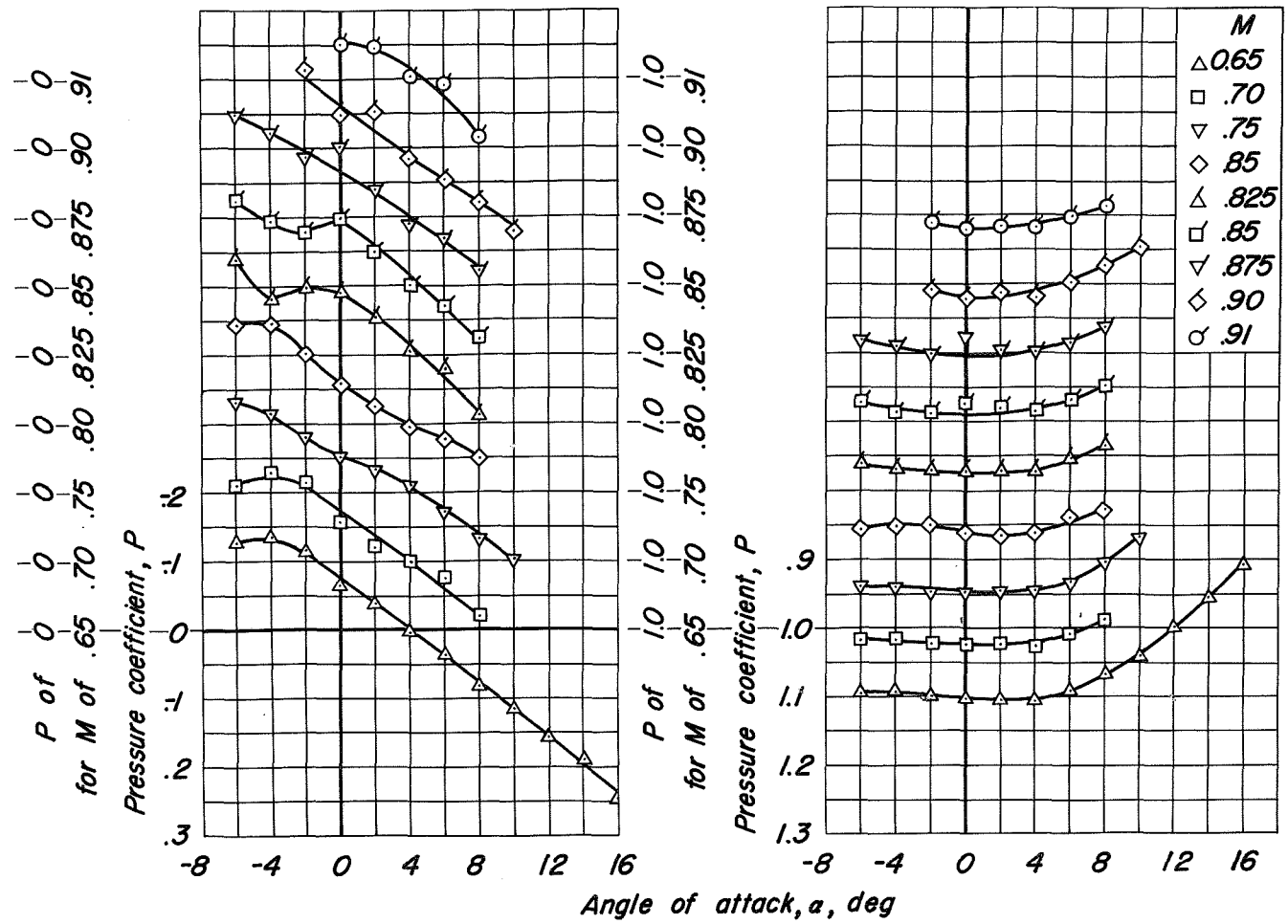

(d) Orifice C'.

(e) Orifice E'.

Figure 23.— Concluded.

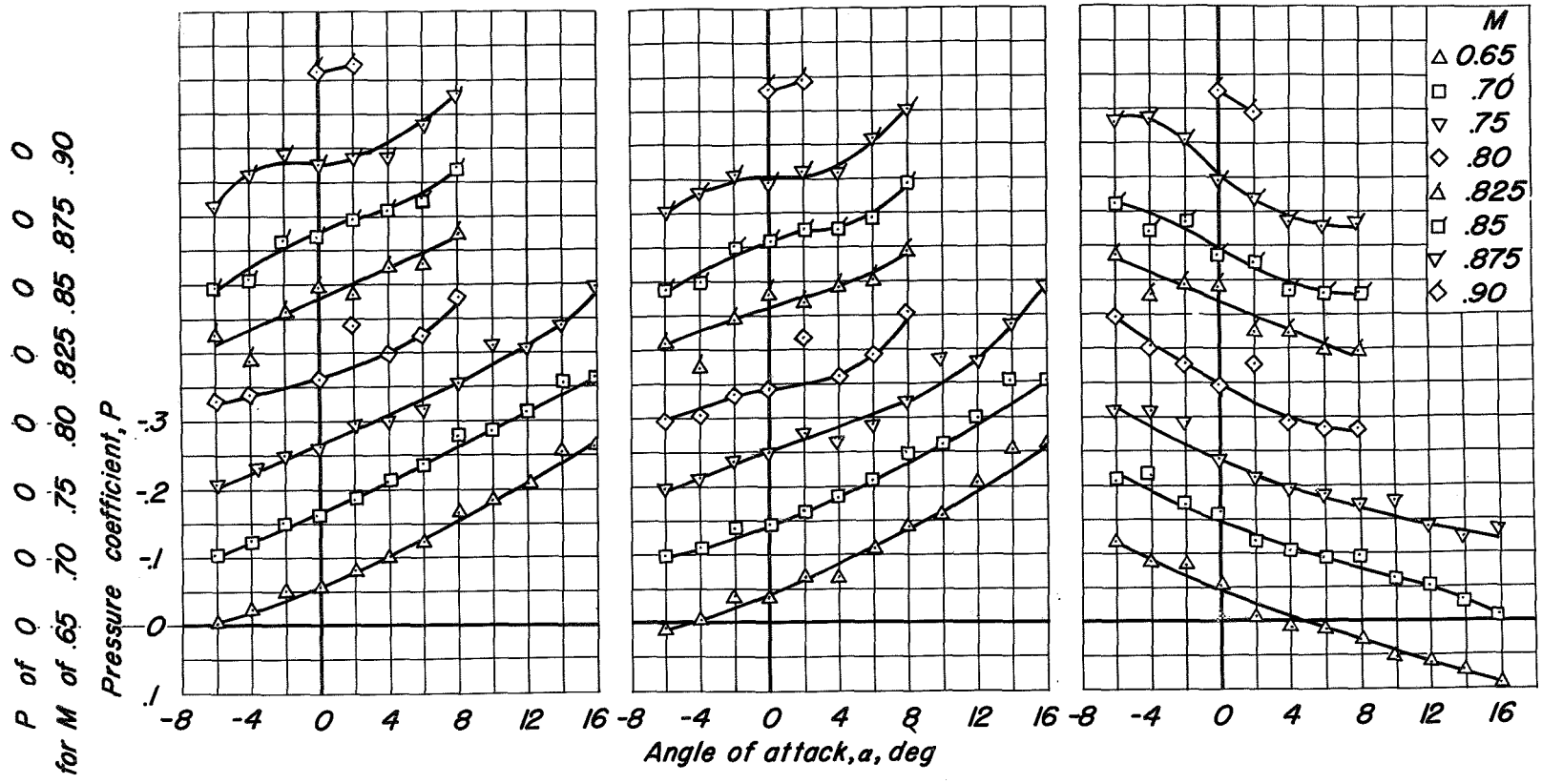

(a) Orifice A. (b) Orifice B. (c) Orifice C.

Figure 24.— Variation of pressure coefficient with angle of attack at various nose orifices of the alternate nose. Orifices 45° to vertical plane as shown in figure 2(a).

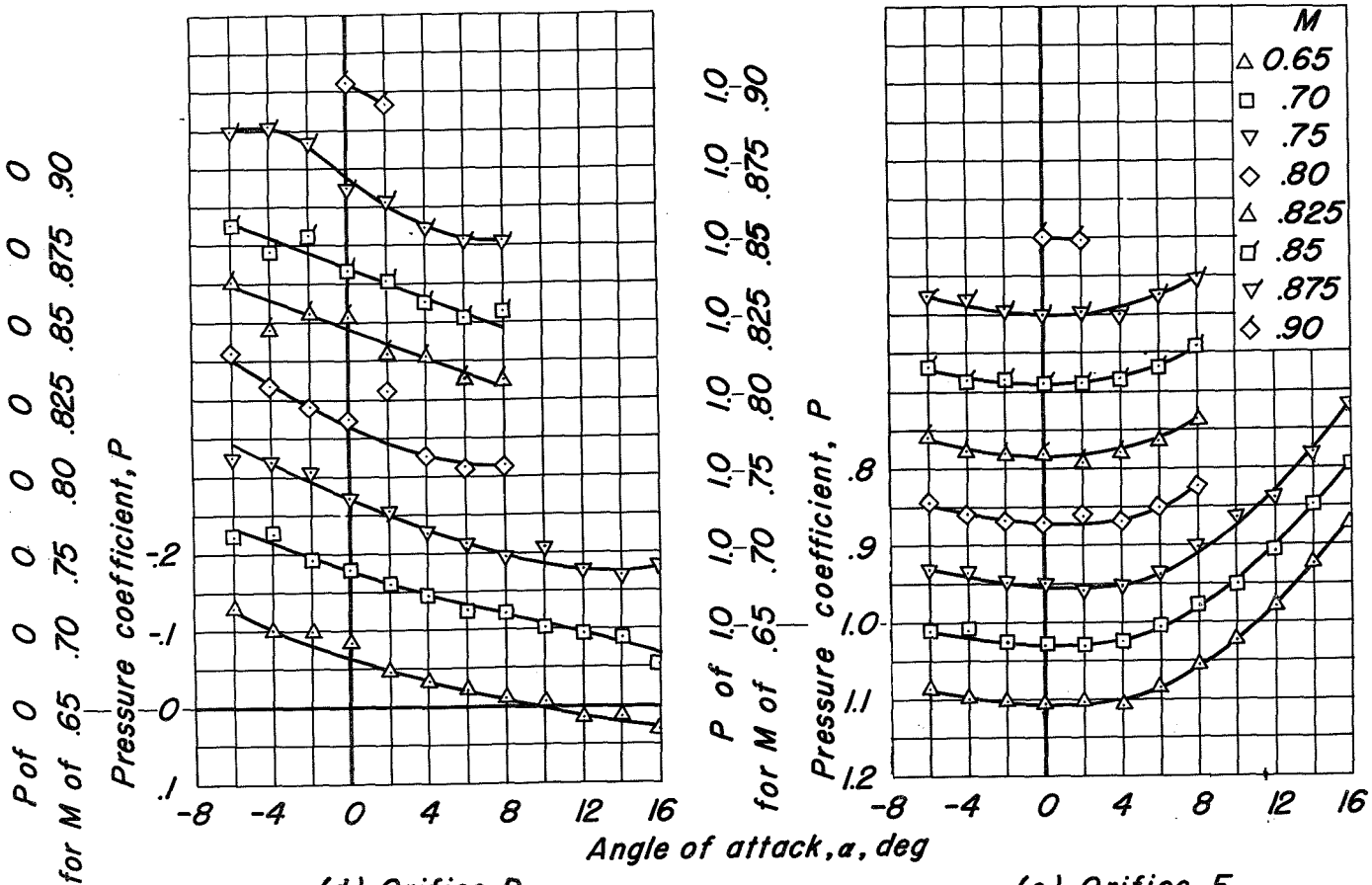

(d) Orifice D. (e) Orifice E.

Figure 24.— Concluded.